Monthly Notices
of the
ROYAL ASTRONOMICAL SOCIETY

MNRAS **454,** 4250–4266 (2015) doi:10.1093/mnras/stv2267

The metal and dust yields of the first massive stars

Stefania Marassi,[1⋆] Raffaella Schneider,[1] Marco Limongi,[1,2] Alessandro Chieffi,[3] Marco Bocchio[1,4] and Simone Bianchi[4]

[1]*INAF/Osservatorio Astronomico di Roma, Via di Frascati 33, I-00040 Monteporzio, Italy*
[2]*Kavli Institute for the Physics and Mathematics of the Universe, Todai Institutes for Advanced Study, The University of Tokyo, Kashiwa 277-8583, Japan*
[3]*INAF/IASF, Via Fosso del Cavaliere 100, I-00133 Roma, Italy*
[4]*INAF/Osservatorio Astrofisico di Arcetri, Largo Enrico Fermi 5, I-50125 Firenze, Italy*

Accepted 2015 September 29. Received 2015 September 21; in original form 2015 May 12

ABSTRACT

We quantify the role of Population (Pop) III core-collapse supernovae (SNe) as the first cosmic dust polluters. Starting from a homogeneous set of stellar progenitors with masses in the range [13–80] $M_\odot$, we find that the mass and composition of newly formed dust depend on the mixing efficiency of the ejecta and the degree of fallback experienced during the explosion. For *standard* Pop III SNe, whose explosions are calibrated to reproduce the average elemental abundances of Galactic halo stars with [Fe/H] < -2.5, between 0.18 and 3.1 $M_\odot$ (0.39–1.76 $M_\odot$) of dust can form in uniformly mixed (unmixed) ejecta, and the dominant grain species are silicates. We also investigate dust formation in the ejecta of *faint* Pop III SN, where the ejecta experience a strong fallback. By examining a set of models, tailored to minimize the scatter with the abundances of carbon-enhanced Galactic halo stars with [Fe/H] < -4, we find that amorphous carbon is the only grain species that forms, with masses in the range 2.7×10^{-3}–$0.27\,M_\odot$ (7.5×10^{-4}–$0.11\,M_\odot$) for uniformly mixed (unmixed) ejecta models. Finally, for all the models we estimate the amount and composition of dust that survives the passage of the reverse shock, and find that, depending on circumstellar medium densities, between 3 and 50 per cent (10–80 per cent) of dust produced by *standard* (*faint*) Pop III SNe can contribute to early dust enrichment.

Key words: stars: low-mass – supernovae: general – ISM: clouds – Galaxy: halo – galaxies: evolution.

1 INTRODUCTION

Dust grains play a fundamental role in the evolution of stellar populations at high redshift. Population III stars (hereafter Pop III), so far undetected, are responsible of the first chemical enrichment of the high-redshift interstellar medium (ISM). Given the current theoretical limits on the mass of the first stars (Hosokawa et al. 2011, 2012), early metal enrichment is likely to be mostly driven by the first core-collapse supernovae (SNe), with a possible contribution from more massive pair-instability SNe (although this may strongly depend on the poorly constrained tail of the stellar initial mass function; Hirano et al. 2014, 2015; Susa, Hasegawa & Tominaga 2014).

Yet, the amount and properties of grains that can be injected in the high-redshift ISM and contribute to the enrichment depend on the dust condensation efficiencies in SN ejecta and on the destruction suffered by thermal and non-thermal sputtering during the passage of the reverse shock of the SN, on time-scales of 10^4 yr (Bianchi & Schneider 2007; Nozawa et al. 2007). Depending on the density of the circumstellar medium where the explosion takes place, the mass fraction of newly formed dust that is able to survive ranges between 2 and 20 per cent for circumstellar medium densities in the range $10^{-25} < \rho/(\mathrm{g\,cm^{-3}}) < 10^{-23}$, which corresponds to number densities in the range $0.06 < n_{\rm ISM}/(\mathrm{cm^{-3}}) < 6$ (Bianchi & Schneider 2007; Nozawa et al. 2007; Silvia, Smith & Shull 2010, 2012; Marassi et al. 2014). In addition, the passage of the reverse shock significantly alters the grain size distribution and modifies the grain cross-section, changing the dust cooling efficiency (Schneider & Omukai 2010).

Dust formation in SN ejecta has been investigated following two different methods: classical nucleation theory (CNT) and a chemical kinetic approach (Cherchneff & Dwek 2009, 2010; Sarangi & Cherchneff 2013). Theoretical models, developed in the framework of CNT, have shown that dust formation can take place in SN ejecta a few hundred days after the explosions and provide predictions on the mass, composition and size distribution of the newly formed grains (Kozasa, Hasegawa & Nomoto 1989, 1991; Todini & Ferrara 2001; Nozawa et al. 2003, 2008, 2010, 2011; Schneider, Salvaterra & Ferrara 2004; Bianchi & Schneider 2007). These

⋆ E-mail: stefania.marassi@oa-roma.inaf.it

models predict dust masses ≈[0.2–0.6] $M_\odot$ for SN progenitors with masses [12–40] $M_\odot$ and metallicities [0.1–1] $Z_\odot$ (Schneider et al. 2014), in agreement with the dust mass inferred from recent *Herschel* and ALMA observations of SN 1987A (Matsuura et al. 2011; Indebetouw et al. 2014) and Cas A (Barlow et al. 2010). Although in the past the applicability of CNT in astrophysical context has been questioned (Donn & Nuth 1985; Cherchneff & Dwek 2009), mainly due to the assumption of chemical equilibrium at nucleation, recently Paquette & Nuth (2011) showed that this assumption has a lower impact on the grain mass and size distribution than previously thought. Similarly, Nozawa & Kozasa (2013) demonstrated that CNT is a good approximation in SN ejecta, at least until the collisional time-scales of the key molecule is much smaller than the time-scale with which the supersaturation ratio increases.

The goal of this study is to investigate the role of Pop III core-collapse SN as dust polluters, adopting a homogeneous set of metal-free progenitors with masses in the range [13–80] $M_\odot$. Under the assumption that the observed metal-poor stars likely formed from gas clouds enriched by Pop III SNe, we use properly calibrated SN explosion models (Chieffi & Limongi 2002) to calculate the formation of dust in the ejecta, applying CNT and accounting for the process of grain growth. We quantify the impact of ejecta mixing on the final dust masses and grain size distributions, analysing both uniformly mixed models within the helium core and unmixed/stratified cases. To obtain a more realistic estimate of the dust mass that is able to enrich the ISM, we also consider the effects of the reverse shock (Bianchi & Schneider 2007).

Motivated by the observed surface elemental abundances of Carbon-Enhanced Metal-Poor (CEMP) stars, i.e. stars with an observed overabundance of light elements compared to Fe and – in particular – with [C/Fe]>1 (Beers & Christlieb 2005), we also investigate dust formation in the ejecta of *faint* Pop III SN, where the ejecta experience mixing and fallback (Umeda & Nomoto 2002, 2003). Recently, Marassi et al. (2014) showed that dust can be produced in faint Pop III SN ejecta (see Kochanek 2014 for dust formation in solar metallicity faint SNe).

Here, we extend this previous analysis and we simulate a large set of faint Pop III SN models, searching for a combination of mixing and fallback that provides the best fit to the observed abundance pattern of all currently known C-enhanced hyper iron-poor stars (Beers & Christlieb 2005; Yong et al. 2013; Ishigaki et al. 2014; Keller et al. 2014). For these faint SN models we also explore the impact, on the final dust masses, of ejecta mixing and reverse shock.

The plan of the paper is as follows. In Section 2 we briefly summarize the Bianchi & Schneider (2007) dust nucleation model and we describe the upgraded molecular network. In Section 3 we illustrate the main features of Pop III SN progenitors that are modelled using FRANEC stellar evolutionary code (Limongi & Chieffi 2006, 2012) and their calibration. In Section 4 we present the resulting dust yields for Pop III core-collapse SNe. In Section 5 we describe how we construct, using the mixing and fallback procedure (Umeda & Nomoto 2002), faint Pop III ejecta calibrated with the same procedure described in Marassi et al. (2014). In Section 6 we show the results on dust yields obtained in Pop III faint SN ejecta. In Section 7 we discuss all the results and their dependence on the fallback, ejecta mixing and reverse shock, and we draw our conclusions. In the appendix we present our final dust data grids that will be available to the community.[1]

[1] The resulting dust and metal yields will be available in electronic format for interested researchers upon request.

2 DUST FORMATION MODEL

To model dust formation in SN ejecta we follow the Bianchi & Schneider (2007) model, where CNT in steady state conditions was applied (see Nozawa et al. 2003; Bianchi & Schneider 2007 and references therein). For our calculation, we use a previously developed code that has been applied to core-collapse (Todini & Ferrara 2001; Bianchi & Schneider 2007) and pair-instability SNe (Schneider et al. 2004). This theoretical model has allowed us to successfully reproduce the dust masses observed in SNe and young SN remnants (Schneider et al. 2014; Valiante & Schneider 2014). In Bianchi & Schneider (2007) the chemistry of molecular formation is implemented following Todini & Ferrara (2001), but relaxing the assumption of steady state. In the gas phase, the formation of carbon monoxide (CO) and silicon oxide (SiO) was assumed to be driven by radiative association reactions and destroyed by Compton electrons coming from radioactive decay of ^{56}Co. Seven different grain species are formed in SN ejecta: amorphous carbon (AC), iron, corundum (Al_2O_3), magnetite (Fe_3O_4), enstatite ($MgSiO_3$), forsterite (Mg_2SiO_4) and quartz (SiO_2). In this work, we follow the formation of the above grain species assuming that seed clusters are formed by a minimum of two monomers, which subsequently grow by accretion of other monomers. The accretion process is regulated by the collisional rate of the key species and depends on the sticking coefficient (defined as the probability that an atom colliding with a grain will stick to it) which we have assumed equal to 1 for all grain species. A discussion of the dependence of the dust yields on these two parameters can be found in Bianchi & Schneider (2007), where it is also possible to find a description of the adopted properties of SN dust species to which we refer for more details.

2.1 Upgraded molecular network

It is well known that CO and SiO molecules play a fundamental role in the dust formation process: CO formation subtracts C-atoms and limits the formation of AC grains. SiO is required to form silicates, such as $Mg_2SiO_4$and $MgSiO_3$. Due to the important role of molecules in the dust formation pathway, we have enlarged our molecular network taking into account other formation/destruction processes involving CO/SiO molecules and their interactions with O_2 and C_2. These molecular processes are crucial in subtracting gas-phase elements from the ejecta (in particular oxygen and carbon, which are very abundant; see left-hand panel of Fig. 2), that otherwise are free to form dust. We follow the evolution of CO, SiO, O_2 and C_2 which form through different channels (reaction rates), respectively: (i) radiative association reactions where the formation of molecules takes place through the emission of a photon which carries off the excess energy released during the formation process; (ii) bimolecular, neutral–neutral reactions that involve molecules and atoms. For these two-body reactions, the formation rates of molecules $k(T)$ are given by the usual Arrhenius-type expression,

$$k(T) = \alpha \left[\frac{T}{300\ \mathrm{K}}\right]^{\beta} \exp\left[\frac{-\gamma}{T}\right]\ \mathrm{cm^3\ s^{-1}}, \quad (1)$$

where T is the temperature of the ejecta gas in K and γ the activation energy in K. In Table 1 we report the rates expressed in the Arrhenius form according to the UMIST data base for astrochemistry 2012 (McElroy et al. 2012).[2] This data base is a compilation of molecular rates that have different origin, some are theoretically calculated,

[2] http://udfa.ajmarkwick.net

Table 1. Molecular processes considered in this work: the rate coefficients are taken from the UMIST data base for astrochemistry 2012; where the origin of the reaction rates is different the corresponding reference is indicated.

Type	Reaction	Rate coefficient	Reference
RA1	$C + O \rightarrow CO + h\nu$	$k_{RA1} = 1.58 \times 10^{-17}(T/300)^{0.3}\exp(-1297.4/T)$	Dalgarno, Du & You (1990)
RA2	$Si + O \rightarrow SiO + h\nu$	$k_{RA2} = 5.52 \times 10^{-18}(T/300)^{0.3}$	UMIST
RA3	$C + C \rightarrow C_2 + h\nu$	$k_{RA3} = 4.36 \times 10^{-18}(T/300)^{0.3}\exp(-161.3/T)$	Andreazza & Singh (1997)
RA4	$O + O \rightarrow O_2 + h\nu$	See text	Babb & Dalgarno (1995)
NN1	$C + O_2 \rightarrow CO + O$	$k_{NN1} = 5.56 \times 10^{-11}(T/300)^{0.4}\exp(26.90/T)$	UMIST
NN2	$O + C_2 \rightarrow CO + C$	$k_{NN2} = 2.0 \times 10^{-10}(T/300)^{-0.1}$	UMIST
NN3	$C + CO \rightarrow C_2 + O$	$k_{NN3} = 2.94 \times 10^{-11}(T/300)^{0.5}\exp(-58\,025/T)$	UMIST
NN4	$O + CO \rightarrow O_2 + C$	See text	–
NN5	$Si + CO \rightarrow SiO + C$	$k_{NN6} = 1.30 \times 10^{-9}\exp(-34\,513/T)$	UMIST
NN6	$C + SiO \rightarrow CO + Si$	$k_{NN8} = 1.00 \times 10^{-16}$	UMIST

others are directly measured in the laboratory. Clearly, there is a degree of uncertainty related to the rate calculations: in some cases we decided to refer to other rate estimates present in the literature that are more robust. This is the case for the radiative association rate coefficient of O_2 (RA4), for which we have chosen to fit the expression of the rate coefficient, as a function of temperature, obtained from theoretical calculations in Babb & Dalgarno (1994). In addition, we found that the neutral backward reaction NN4 is negligible (Omukai, private communication).

In standard nucleation theory, dust condensation is described in terms of a nucleation current that depends on the abundance of the key species. Hence, contrary to other studies which adopt a chemical kinetic approach (Cherchneff & Dwek 2009, 2010; Sarangi & Cherchneff 2015), we do not follow the formation of carbon chains as a pathway to solid carbon clusters. Thermal fragmentation of the chains through collisions with gas particles, in addition to oxidation reactions similar to NN2, may limit the formation of carbon chains. However, if all C_2 were to contribute to carbon dust formation, the estimated carbon dust mass would need to be corrected upwards by M_{C_2}.

We take into account the destruction due to Compton electrons coming from the ^{56}Ni decay in the ejecta. As observed in SN 1987A, destruction by Compton electrons has a deep impact on the ejecta chemistry. As shown by Woosley, Pinto & Hartmann (1989), the explosion of SN 1987A has produced ^{56}Ni which decays in $\sim$6 d into ^{56}Co; the subsequent decay of ^{56}Co into ^{56}Fe deposits energy as γ-rays in the SN ejecta, powering the observed light curve. In SN 1987A, the emitted light curve is very well reproduced if 0.075 $M_\odot$ mass of ^{56}Co was ejected during the SN explosion.

Here we assume molecules to be destroyed by the impact with energetic electrons produced by the radioactive decay of ^{56}Co, with a rate coefficient k_d that depends also on the mean energy per ion pair W_i. According to Woosley et al. (1989), this rate coefficient can be estimated as follows: the thermalized γ-ray energy input rate for a given ^{56}Co mass is given by

$$L_\gamma = 9.54 \times 10^{41} \left(\frac{M_{^{56}\mathrm{Co}}}{0.075\,\mathrm{M}_\odot} \right) f_\gamma(k_{56}) \mathrm{e}^{-t/\tau_{56}}\ \mathrm{erg\ s^{-1}}, \quad (2)$$

where 0.075 $M_\odot$ was the adopted mass of ^{56}Co produced in the original Woosley et al. (1989) model, $\tau_{56} = 111.26$ d is the e-folding time of ^{56}Co decay, and the function f_γ is the deposition function and it is given by 1 minus the fraction of energy that escapes in photons in the X-ray and γ-ray bands,

$$f_\gamma(k_{56}) = 1 - \mathrm{e}^{[-k_{56}\phi_0(t_0/t)^2]}, \quad (3)$$

where $\phi_0 = \phi(t_0)$ represents the column depth of the SN at some fiducial time t_0 (for $t_0 = 10^6$ s $\phi_0 = 7 \times 10^4$ g cm^{-2}) and $k_{56} = 0.033$ cm^2 g^{-1} is an average opacity to γ-rays from ^{56}Co decay. The above-quoted values of k_{56} and ϕ_0 have been derived by Woosley et al. (1989) for SN 1987A and we will assume these to hold for all the explored SN progenitors. In particular, we assume that once a γ-ray Compton scatters with electrons, it is completely absorbed. Thus, the L_γ can be considered as the electron energy input and the energy transferred to a single gas particle per unit time can be computed as

$$L_e = L_\gamma / N_{part}, \quad (4)$$

where N_{part} is the number of gas particles in the ejecta. To compute the destruction rate, k_d, it is necessary to divide L_e by the mean energy per dissociation, W_i. For example, to compute the destruction rate of neutral CO we divide L_e by the mean energy per dissociation $W_{i,CO}$, obtaining

$$k_d(\mathrm{CO}) = L_e / W_i \qquad \mathrm{s^{-1}}. \quad (5)$$

Finally, we assume that all the radioactive energy is deposited uniformly in the ejecta. As it will be clear in what follows, the efficiency of molecule formation/destruction processes depends on the chemical composition and on the thermodynamics of the ejecta. In Section 4, we give a detailed description of the relevant processes for some selected SN models.

3 POP III SN PROGENITORS' MODELS

The pre-SN models adopted in this paper are the ones presented and discussed in details in Limongi & Chieffi (2012). These models span a range of mass between 13 and 80 $M_\odot$ and have a pristine Big Bang initial composition. The evolution of these models has been followed from the pre-main sequence up to the onset of the iron core collapse by means of the FRANEC stellar evolutionary code (Limongi & Chieffi 2006). The explosion of the mantle and the consequent explosive nucleosynthesis have been computed in the framework of the 'artificially induced explosion'. Then, for each model, the mass cut (M_{cut}), i.e. the mass coordinate which separates the final remnant from the ejected portion of the mantle, has been fixed by requiring a best fit to the element abundance pattern of the Cayrel average star, as extensively described in Limongi & Chieffi (2012). In Table A1 we summarize the main properties of the SN explosion models.

We construct the Pop III ejecta models, requiring that the thermal, dynamical and chemical evolution of the ejecta evolve consistently with the explosive nucleosynthesis simulation (see next section for

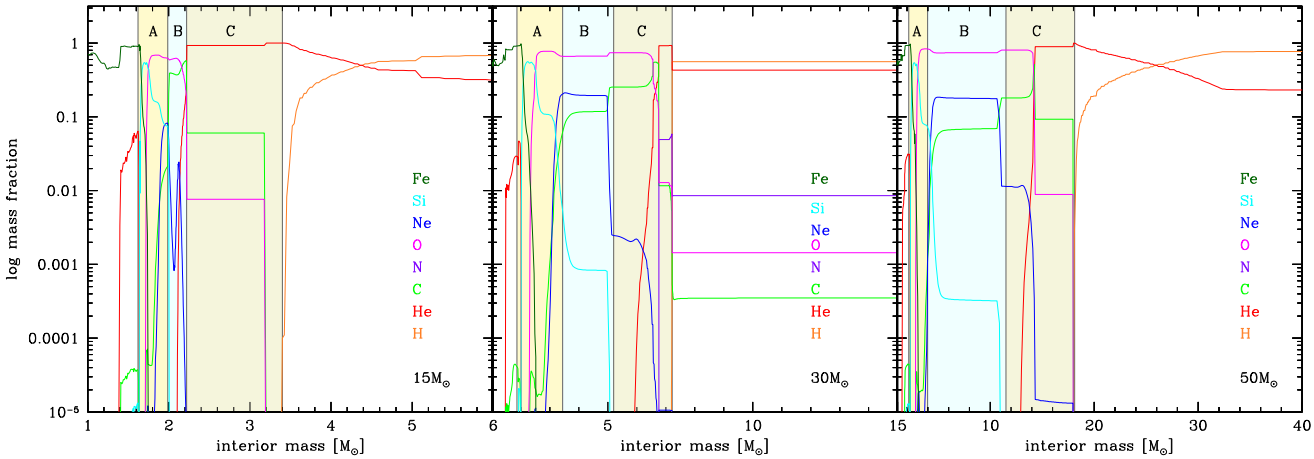

Figure 1. Pre-SN chemical structure for three selected models: 15 $M_\odot$ (left-hand panel), 30 $M_\odot$ (central panel), 50 $M_\odot$ (right-hand panel). The shaded region extends up to the mass coordinate of the He core. Different shaded regions indicate the layers that we will consider in the unmixed SN models (layers A, B and C from left to right).

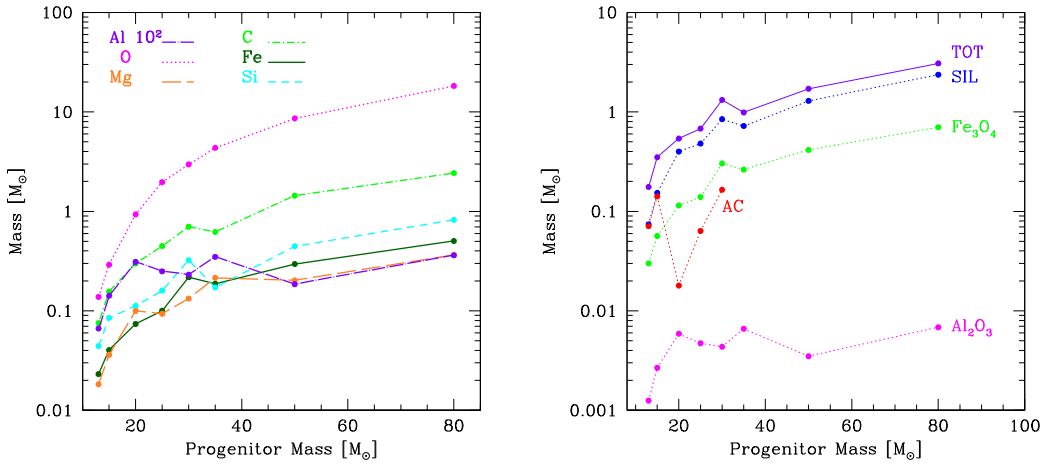

Figure 2. Left-hand panel: initial metal abundances in the ejecta of the adopted SN models as a function of the progenitor stellar mass (the abundance of Al has been multiplied by 10^2). Right-hand panel: mass of dust grains, before the passage of the reverse shock, as a function of the progenitor mass. SIL is the total mass in silicates, including Mg_2SiO_4, $MgSiO_3$ and SiO_2.

details). We have performed dust formation calculations assuming uniform mixing of the elemental abundances in the He core. However, due to the uncertainties related to the efficiency of mixing in metal-free SNe (Joggerst, Woosley & Heger 2009; Heger & Woosley 2010), for some models we also present the results obtained assuming unmixed ejecta. In Fig. 1 we show the chemical structure (elemental mass fraction) as a function of the mass coordinate for three selected pre-SN models, 15, 30 and 50 $M_\odot$ (for a detailed description of the differences emerging in the convective zones we refer the reader to Limongi & Chieffi 2012). The shaded region extends up to the mass-coordinate of the He core, different colours indicate the layers that we will consider in the unmixed SN models, in Section 4. The left boundary of the innermost shaded region corresponds to the adopted mass-cut coordinate. In the left-hand panel of Fig. 2 we show, for each SN model, the initial abundance of metal species which participate to molecules and dust formation; for all the SN models, the ejecta are very rich in carbon and oxygen and the total mass of metals is an increasing function of the progenitor mass. The ejecta mass $M_{\rm eje}$, as expected, is an increasing function of the progenitor mass and explosion energy (see Table A1).

4 RESULTS: POP III SN DUST YIELDS

This section presents the calculated dust yields that we obtain for Pop III core-collapse SN models. As stated in the previous section, we construct the ejecta models using as initial conditions the thermodynamical properties obtained by the SN explosion simulation outputs (Limongi & Chieffi 2012). The ejecta follow an adiabatic expansion and the temperature evolution is given by

$$T = T_0 \left[1 + \frac{v_{\rm eje}}{R_0}(t - t_{\rm ini})\right]^{3(1-\gamma)}, \quad \text{where } v_{\rm eje} = \sqrt{\frac{10\ E_{\rm expl}}{3\ M_{\rm eje}}} \qquad (6)$$

is the ejecta expansion velocity, $\gamma = 1.41$ is the adiabatic index and T_0 and R_0 are the temperature and radius of the He core at the initial time $t = t_{\rm ini}$. This initial time $t_{\rm ini}$ is fixed by requiring that the gas temperature at the radius of the He core, $R_{\rm He_{core}}$, reaches a temperature of $T_0 = 10^4$ K. For all uniformly mixed SN ejecta models (labelled with the progenitor mass) Table A1 reports the thermodynamical properties, the metal yields of the key elements in the nucleation process, the total amount of dust, the mass of molecules and the mass of dust in each grain species. In what follows, we discuss these results in details.

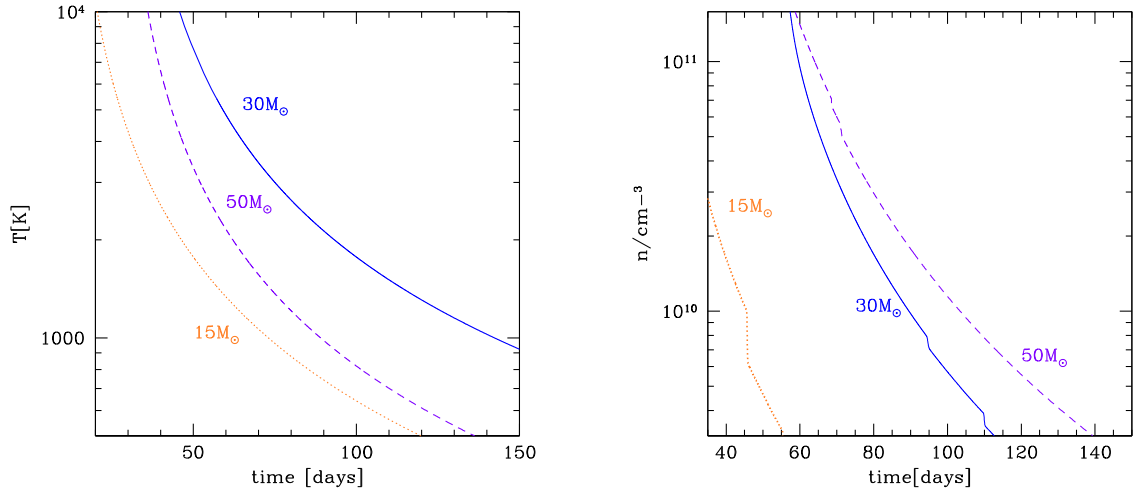

Figure 3. Temperature (left-hand panel) and number density (right-hand panel) evolution for 15 $M_\odot$ (solid), 30 $M_\odot$ (dotted) and 50 $M_\odot$ (dashed) ejecta models.

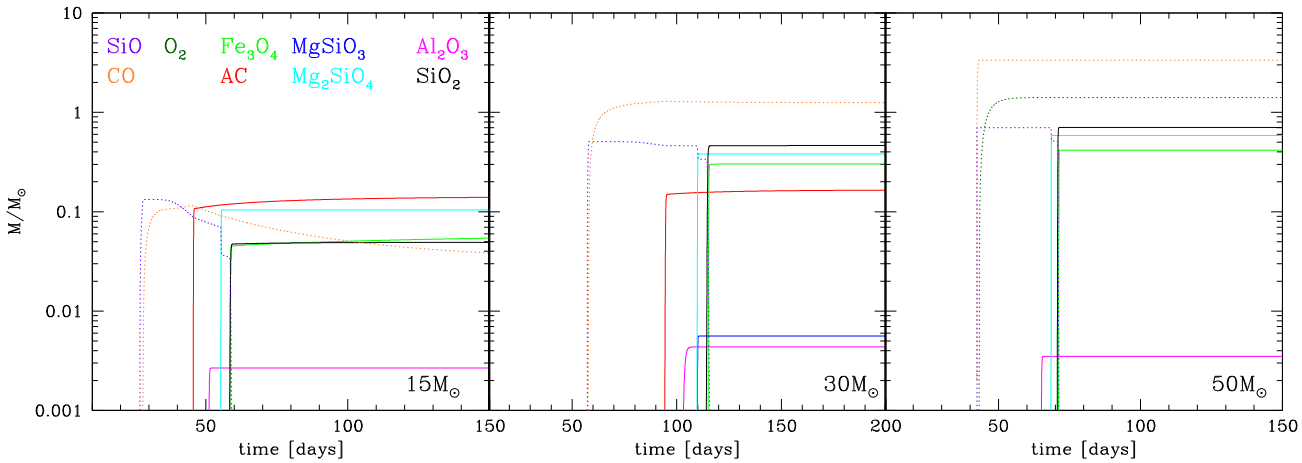

Figure 4. Time evolution of molecular (dashed lines) and dust masses (solid lines) for three metal-free SN progenitors: 15 $M_\odot$ (left-hand panel), 30 $M_\odot$ (middle panel) and 50 $M_\odot$ (right-hand panel).

4.1 Dust formation in uniformly mixed ejecta

In the right-hand panel of Fig. 2 we plot the mass of dust for different grain species as a function of the progenitor mass. We find that (i) the total dust mass produced increases with the progenitor mass, ranging between [0.18–3.1] $M_\odot$, and it is dominated by silicates; (ii) the second most abundant dust species is magnetite, due to the initially high iron abundance present in the ejecta (see left-hand panel of Fig. 2) plus the iron produced by ^{56}Ni decay; (iii) AC forms only in less massive models, with progenitor masses $\lesssim$30 $M_\odot$. This is due to the larger mean ejecta density of more massive progenitors, which increases the rates of the major processes leading to the formation of CO molecules, locking carbon atoms and preventing the formation of AC grains (we will return to this point later); (iv) alumina is the less abundant dust species, reflecting the lower abundance of Al in the ejecta.

Using three representative SN progenitors with masses 15, 30 and 50 $M_\odot$, Fig. 3 shows the evolution of the ejecta temperature and number density: when the He core of the three SN progenitors reaches $T_0 = 10^4$ K, we fixed the initial time $t_{\rm ini}$, which varies between (1.78–3.96) $\times$ 10^6 s (see Table A1). At these initial times, the three ejecta models have radii of 2.44 $\times$ 10^{14}(15 $M_\odot$), 4.68 $\times$ 10^{14}(30 $M_\odot$), and 2.51 $\times$ 10^{14}(50 $M_\odot$) cm, and start the adiabatic expansion with velocities in the range (2960–3086) km s^{-1} (see equation 6), and the temperature decreases. As shown in the right-hand panel of Fig. 3, the initial number densities, n_0 = 7.18 $\times$ 10^{11}(15 $M_\odot$), 7.39 $\times$ 10^{11}(30 $M_\odot$), 1.24 $\times$ 10^{13}(50 $M_\odot$) cm^{-3}, also decrease, showing a step-decrease corresponding to the condensation of the gas-phase elements.

In standard nucleation theory, dust grains condense when the gas becomes supersaturated. For each grain species, this depends on the temperature, density and abundances of the corresponding key element in the ejecta. Fig. 4 shows that grains form between 45 and 120 d after the explosions. Although these time-scales are smaller than the values found by Nozawa et al. (2003) for core-collapse Pop III SN with a 25 $M_\odot$ progenitor, due to the different thermal evolution of the ejecta, the resulting dust masses and grain size distribution are consistent because grain condensation occurs in similar physical conditions.

Molecules form according to the formation/destruction rates described in Section 2.1 and are also partially destroyed by the interaction with Compton electrons produced by destruction reactions rates *D*1–*D*4 (see Table 2), up to the point where the

Table 2. Compton electron destruction reactions and the corresponding mean energy per ion pair W_i.

Type	Reaction	W_i (eV)
$D1$	$CO + e^- \rightarrow C + O + e^-$	$W_{i,CO} = 125$
$D2$	$SiO + e^- \rightarrow Si + O + e^-$	$W_{i,SiO} = 110$
$D3$	$O_2 + e^- \rightarrow O + O + e^-$	$W_{i,O_2} = 125$
$D4$	$C_2 + e^- \rightarrow C + C + e^-$	$W_{i,C_2} = 125$

temperature reaches the condensation window and dust grains start to form. The ejecta density is a strong function of the initial progenitor mass: when the ejecta temperature enters the condensation regime, at around $T \sim 2000$ K, the corresponding density can vary by one order of magnitude, although the dependence on the progenitor mass is not monotonic. Clearly, the chemical evolution of the ejecta depends on the temperature and density at each given time: in Fig. 4 we show, for the same set of SN models, the time dependence of the mass of CO, SiO and of the newly formed dust species.

We start analysing the $15\,M_\odot$ model plotted in the left-hand panel of Fig. 4: CO and SiO start forming at around 27 d after the explosion, when $T \sim 5400\,K$. At this time, the CO formation rate is dominated by the neutral process NN2 that rapidly depletes all the available C_2. SiO molecules form through the neutral channel NN5 and radiative association process RA2. At around 44 d, when $T \sim 2000$ K, the impact with Compton electrons ($D1$) dominates over the other rates and partially destroys CO molecules. The free carbon atoms form AC, which is the first dust species to form, due to its higher condensation temperature. When the temperature decreases to ∼1764 K, alumina grains form, which rapidly deplete aluminium from the ejecta. When T drops to ∼1530 K, Mg_2SiO_4 starts forming – at the same time of $MgSiO_3$ – but Mg_2SiO_4 reaches supersaturation first (because it has the largest nucleation current), rapidly consuming Mg and SiO and inhibiting the growth of $MgSiO_3$. Finally, when $T \sim 1400$ K, Fe_3O_4 and SiO_2 form, depleting completely the remaining SiO and iron from the ejecta.

The central panel of Fig. 4 shows the evolution of molecules and dust grains for the $30\,M_\odot$ model: at ∼57 d, when $5400 \leq T \leq 4250$, the dominant process is radiative association of C_2 which – due to the large oxygen abundance – is then rapidly depleted in CO through the reaction $O + C_2 \rightarrow CO + C$. When T decreases, at around 66 d, the dominant CO formation process becomes radiative association RA1. Around 93 d, the temperature reaches ∼2000 K, nucleation starts, $D1$ efficiently destroys the CO molecule, leaving C atoms free to form AC and – as in the $15\,M_\odot$ model – the CO formation processes are not equally efficient in re-forming the molecule. As a result, AC grains form.

For the more massive model the evolution changes, as shown in the right-hand panel of Fig. 4. The interplay between the larger ejecta density and the richer oxygen content (the mass of oxygen is 18 per cent of the mass of the ejecta) leads to the efficient formation of O_2 molecules through radiative association RA4 and also activates efficiently the bimolecular process NN1, which exceeds the destruction rate $D1$, and becomes the leading process in CO formation. This depletes all the C atoms, inhibiting AC grains condensation. As for the two previous models, at $5400 \leq T \leq 5000$ the main CO formation channel is $O + C_2 \rightarrow CO + C$. When T decreases, it becomes $C + O_2 \rightarrow CO + O$ and it remains so for the subsequent evolution. At 64 d, the nucleation process starts, the grain condensation proceeds as described for the two previous models, because the condensation sequence of the grain species reflects the corresponding condensation temperatures (Todini & Ferrara 2001; Schneider et al. 2004).

We summarize our results on mixed ejecta models in Table A1. The total mass of CO molecules is in the range $[9.60 \times 10^{-3} - 5.66]\,M_\odot$, and increase with the mass of the ejecta due to the initial abundances of oxygen and carbon. SiO molecules form efficiently through NN5 (at early times) and through RA2, but it is completely depleted in silicates at the end of the nucleation process. C_2 molecules are consumed at very early time in the formation process of CO, through the channel NN2. For models less massive than $30\,M_\odot$, O_2 is underproduced (and consumed rapidly in CO formation process), with respect to more massive models. When $M > 30\,M_\odot$ the higher mean ejecta density and oxygen abundance cause radiative association rate RA4 to become the dominant process. This enables a very efficient NN1 reaction rate which overcomes the destruction rate $D1$, locking all carbon atoms in CO molecules.

4.2 Dust formation in unmixed ejecta

The mixing efficiency in SN events is still debated, due to complexity of physical processes associated to core-collapse, such as asphericity and growth of Rayleigh–Taylor instabilities which accompany shock propagation. Besides, these effects are multidimensional and this adds an extra source of uncertainty related to emerging differences in 1D–3D numerical simulations (see Joggerst et al. 2009; Heger & Woosley 2010, and references therein). In particular, the occurrence and the growth of Rayleigh–Taylor instabilities depends on stellar mass and metallicity. It has been shown that the more compact is the star, the more rapid is the reverse shock propagation, giving less time to these hydrodynamical instabilities to grow (Joggerst et al. 2009). For this reason, we have decided to investigate the impact of ejecta mixing on dust formation and we have considered stratified models, as the limiting cases when Rayleigh–Taylor instabilities do not grow. The unmixed case is based on the hypothesis that, due to inefficient mixing, the elemental abundances reflect the pre-SN stratified composition: this means that more internal elements, such as magnesium and silicon are not present or present in very little amount in the more external layers of the star, reducing the probability to form silicates.

In Fig. 1, for each progenitor model, the shaded regions represent the layers that we consider in the stratified models, which extend from the mass-cut coordinate to the outer radius of the He core ($R_{He_{core}}$). The number and extent of the layers have been selected based on the criterium of constant abundances of the relevant elemental species within each layer. Hence, the outer radius of layer A corresponds to the mass coordinate where the Si abundance rapidly drops, and the outer radius of layer B is where the abundance of C (Ne) rapidly increases (decreases).

For the 15, 30 and $50\,M_\odot$ models, we report in Tables A2–A4 the thermodynamical properties, the initial elemental composition, the masses of molecules and dust for all the layers. The time evolution of the molecular and dust masses for each of the three layers of the $30\,M_\odot$ progenitor is shown in Fig. 5. In the stratified ejecta, due to the different temperature evolution of the layers, CO starts to form earlier in the evolution with respect to the corresponding mixed case, and the same is true for SiO, where present. It is worth to note that, compared to the mixed case where O_2 is completely depleted in CO, in layers A and B the O_2 molecule forms, while AC forms only in layer C. Silicates and alumina form in the two internal layers A and B where Al, Si and Mg are present. Magnetite forms only in layer A where iron is present. The total mass of dust for the $30\,M_\odot$ progenitor is $1.2\,M_\odot$, about 90 per cent of the mass formed in the mixed case.

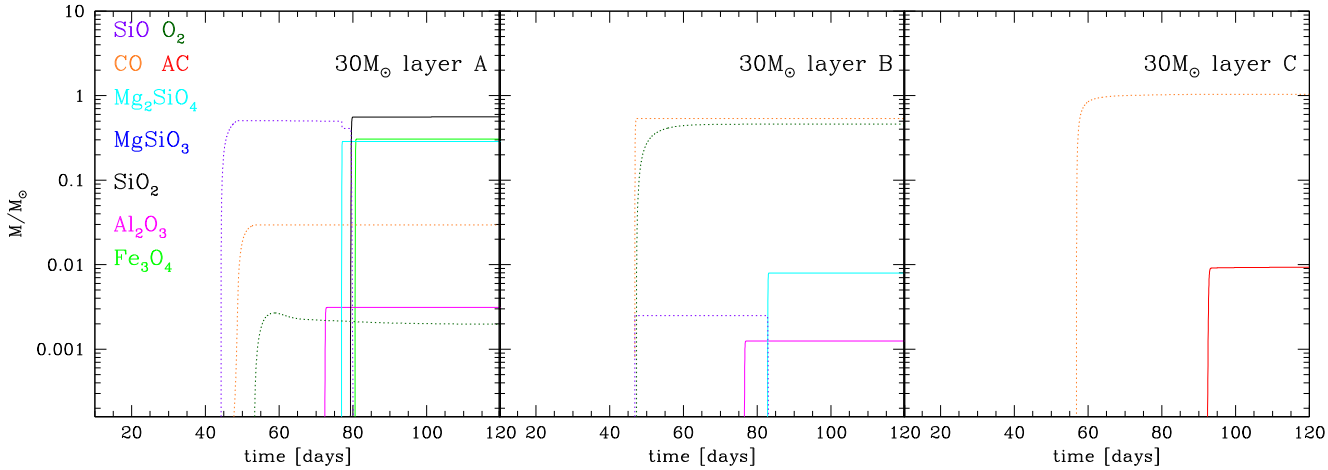

Figure 5. Time evolution of molecular (dashed lines) and dust (solid lines) masses for the 30 $M_\odot$ unmixed model: layer A (left-hand panel), layer B (middle panel), layer C (right-hand panel).

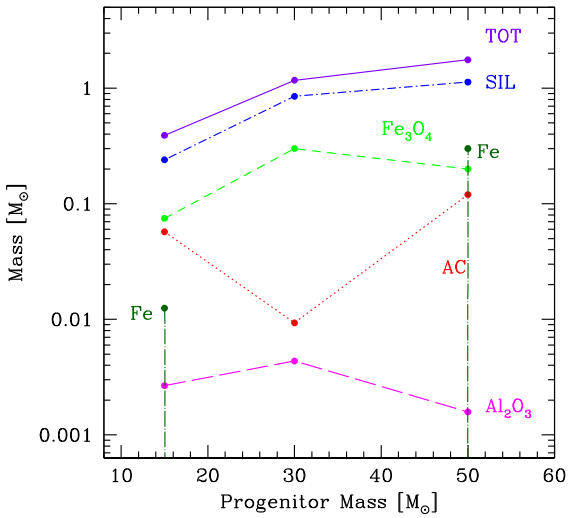

Figure 6. Mass of dust grains, before the passage of the reverse shock, as a function of the progenitor mass for the three selected unmixed models. SIL is the total mass in silicates, including Mg_2SiO_4, $MgSiO_3$ and SiO_2.

Fig. 6 summarizes the results obtained for unmixed ejecta models. The mass of dust for different grain species is shown as a function of the progenitor mass. We find that the total dust mass is in the range [0.39–1.76] $M_\odot$, and it is dominated by silicates. Contrary to the fully mixed cases, for the 15 and 50−$M_\odot$ SN progenitor models, solid iron is able to form due to the initially high iron abundance present in the most internal layer of the ejecta plus the iron produced by ^{56}Ni decay. As a result, in these models the total dust mass formed is ∼3–10 per cent larger than in the mixed case. The CO mass, differently from the mixed case, is not increasing with the progenitor mass, but varies depending on rate formation efficiency which is a function of temperature, mean density and composition of each layer.

4.3 Dust destruction by the reverse shock

To describe the impact of the reverse shock on the dust grains formed inside the expanding ejecta and to estimate the surviving dust mass, we follow the approach described in Bianchi & Schneider (2007) for which we summarize the key points: (i) the dynamics of the reverse shock is treated using Truelove and McKee analytic approximations (Truelove & Mckee 1999) which follow the forward and reverse shock evolution as a function of the main ejecta parameters, such as kinetic energy, $E_{\rm expl}$, ejecta mass, $M_{\rm eje}$, and density of the ISM, $\rho_{\rm ISM}$; (ii) the distribution of dust grains in the ejecta is uniform and the size distribution is the same everywhere; (iii) to quantify the role of $\rho_{\rm ISM}$ we analyse three different cases with $n_{\rm ISM}$ = 0.06 (rev1), 0.6 (rev2) and 6 cm^{-3} (rev3). As previously shown in Todini & Ferrara (2001) and Nozawa & Kozasa (2003), the nucleation and accretion processes lead to a typical lognormal grain size distribution: in the right-hand panel of Fig. 7 we show the grain size distribution of the 30−$M_\odot$ SN model with mixed ejecta, before and after the passage of the reverse shock. The grain sizes are in the range [10^{-3}−0.5] μm, depending on the grain species and on the SN ejecta models. Since AC is the first grain species to condense, it has sizes larger than the other grains because grain accretion is more efficient at larger densities. For the same reason, alumina grains have the smallest sizes due to the low initial abundance of Al in the ejecta. As a result, the latter grain species is almost completely destroyed by the reverse shock, while the other grain species suffer a partial destruction, with the grain size distribution flattening towards smaller grain sizes.

The dust mass which survives the impact of the reverse shock is reported for all mixed SN models in Table A5, where we have also specified the dust mass of each grain species. In the left-hand panel of Fig. 7 we show, for all Pop III mixed SN models, from top to bottom, the total mass of dust at the end of nucleation and after the impact of the reverse shock for the three increasing values of $n_{\rm ISM}$. In the worst scenario, when the SNe explode in the densest ISM, the reverse shock travels faster and encounters a higher density gas inside the ejecta, increasing the sputtering and causing that only ∼3 per cent of the newly formed dust mass survives. Clearly, the percentage of surviving dust depends on the ejecta model and ranges from 48 to 3 per cent. In Fig. 8 the same histograms are reproduced for 15, 30 and 50−$M_\odot$ mixed models, showing the impact of the reverse shock on the different grain species. We can see that alumina grains are completely destroyed. Depending on $n_{\rm ISM}$, after the passage of the reverse shock, we see that (i) in the 15 $M_\odot$ model the dominant species becomes AC, differently from the no-rev case, where AC and silicates have comparable masses; (ii) in the 30 $M_\odot$ model silicates always dominate the mass of dust; however, the smaller destruction suffered by AC grains, compared

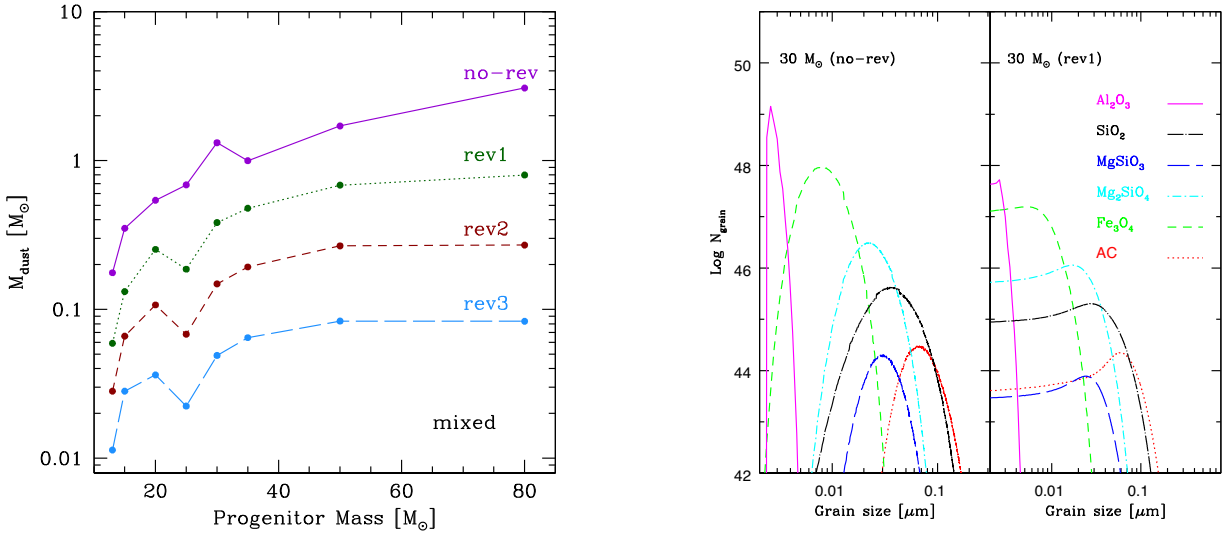

Figure 7. Left-hand panel: the mass of dust at the end of nucleation, and after the passage of a reverse shock of increasing intensity for all the mixed SN models considered in this study. From top to bottom: no reverse shock models (no-rev), models with a circumstellar medium density of $n_{ISM} = 0.06$ (rev1), 0.6 (rev2) and 6 cm^{-3} (rev3). Right-hand panel: size distribution function of the grains for a 30 $M_\odot$ progenitor model before (no-rev, left) and after the passage of the reverse shock (rev1, right).

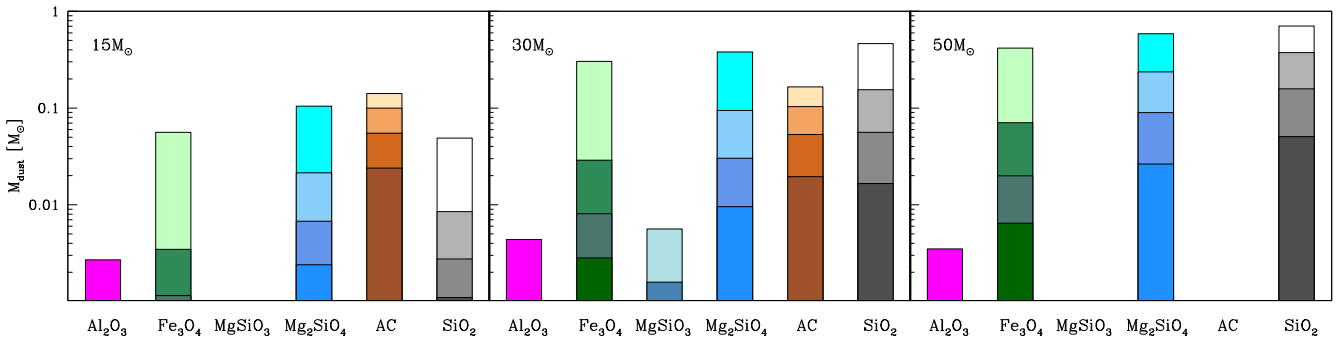

Figure 8. Histograms showing the mass of dust in the different compounds at the end of nucleation, and after the passage of a reverse shock of increasing intensity for three mixed SN models of 15, 30 and 50 $M_\odot$. From top to bottom: no reverse shock models (no-rev), models with a circumstellar medium density of $n_{ISM} = 0.06$ (rev1), 0.6 (rev2) and 6 cm^{-3} (rev3).

to other grain species, alters the original dust composition and after the passage of the reverse shock the mass of AC and silicates are comparable and AC grains are more abundant than Fe_3O_4 grains; (iii) in the 50 $M_\odot$ model, silicates dominate all the grain species, as in the no-rev case.

Fig. 9 illustrates the dust mass which survives to the impact of the reverse shock for the three selected unmixed models (see also Table A6 for the amount of grains of different species in the three layers). After the passage of the reverse shock, depending on the density of the ISM and on the progenitor mass, the percentage of surviving dust ranges from 16 to 100 per cent. Also, compared to the fully mixed models, we note that in each case dust is destroyed to a minor degree. In fact, in all the three unmixed models, most of the dust mass is produced in the innermost layer (layer A). At the time the reverse shock reaches this region of the ejecta, density is low and the effect of the reverse shock is less destructive. In Table A6 we note that, while layer B and C are highly affected by the passage of the reverse shock, dust in layer A survives in large quantities and represents almost the totality of the survived dust mass. These calculations have been performed with an updated version of the code by Bianchi & Schneider (2007) which considers also stratified ejecta, taking into account the gas (density, temperature, elemental

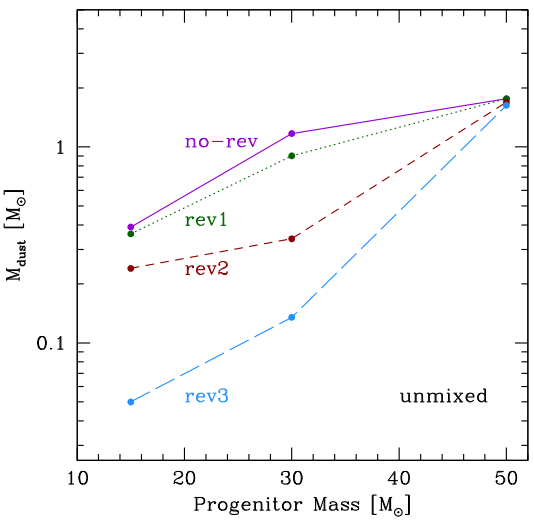

Figure 9. Mass of dust grains, after the passage of the reverse shock, as a function of the progenitor mass for the three selected unmixed models. From top to bottom: no reverse shock models (no-rev), models with a circumstellar medium density of $n_{ISM} = 0.06$ (rev1), 0.6 (rev2) and 6 cm^{-3} (rev3).

abundances) and dust (composition, size distribution) properties in each shell depending on the position within the ejecta.

These results suggest that the effect of the reverse shock must be taken into account in order to have a reliable estimate of the final dust mass and composition.

5 POP III FAINT SN PROGENITORS

We know from observations that a fraction of ∼10–20 per cent of iron-poor stars observed in the Galactic halo with [Fe/H] < −2 are carbon rich (Yong et al. 2013; Placco et al. 2014 and references therein). Most notably, the observed frequency of CEMP stars that do not show overabundances of neutron-capture elements, the so-called CEMP-no stars, increases to 80 per cent at [Fe/H] < −4, with interesting implications for chemical evolution models and the formation pathway of these hyper iron-poor stars (de Bennassuti et al. 2014).

Different scenarios have been proposed to explain the observed elemental abundances of CEMP-no stars (see Norris et al. 2013 and references therein). Among these are, stellar winds of fast-rotating massive stars (Maeder, Meynet & Chiappini 2015), a single Pop III SN, experiencing mixing and fallback after the explosion (Umeda & Nomoto 2002; Iwamoto et al. 2005; Tominaga, Umeda & Nomoto 2007; Tominaga 2009; Heger & Woosley 2010; Yong et al. 2013; Ishigaki et al. 2014; Marassi et al. 2014; Tominaga, Iwamoto & Nomoto 2014), or in terms of an almost failed Pop III SN (with a large fallback) exploding in an environment pre-enriched by one or more normal Pop III SNe (Limongi, Chieffi & Bonifacio 2003).

In Marassi et al. (2014) we interpreted the surface element abundances of SMSS J031300, the recently discovered CEMP-no stars with [Fe/H] <−7.1 (Keller et al. 2014), in the framework of the mixing–fallback scenario. In particular, in that paper dust formation in the ejecta of Pop III faint SNe was investigated for the first time, showing that – depending on the extent of mixing experienced by the ejecta and on the partial destruction by the SN reverse shock – between 0.025 and 2.25 $M_\odot$ of carbon dust forms. These dust masses are large enough to activate dust-driven fragmentation (Schneider et al. 2012) in the parent star-forming cloud of SMSS J031300, even accounting for the dilution and mixing of the SN ejecta with the surrounding pristine gas (Marassi et al. 2014).

In this section, we use the same procedure applied in Marassi et al. (2014) to estimate the mass and composition of dust that forms in the ejecta of faint Pop III SNe. The SN models have been selected by comparing the predicted elemental yields with the observed surface elemental abundances of the four C-enhanced, hyper iron-poor stars currently known, namely HE1327−2326 (Frebel et al. 2005), HE0107−5240 (Christlieb et al. 2002), HE0557−4840 (Norris et al. 2007) and SMSS J031300 (Keller et al. 2014). For each of these, we vary the mixing and fallback efficiencies so as to minimize the scatter between the observed abundance pattern and the elemental yields predicted by Pop III SN models (Limongi & Chieffi 2012).[3]

The surface chemical abundances of HE1327−2326, HE0107−5240 and HE0557−4840 have been taken from the recent compilation by Norris et al. (2013, see their table 4; here we normalize to the solar abundances of Asplund et al. 2009), which are based on high-resolution data, but are determined using 1D, LTE model-atmosphere analysis. The upper limit on silicon for HE1327–2326, HE0107–5240 and HE0557–4840 is taken from Yong et al. (2013). For consistency, we consider the observed elemental abundances of SMSS J031300 as derived from 1D model atmosphere (Marassi et al. 2014). In Fig. 10 we show the comparison between the observed elemental abundances and the best-fitting models for each of the four stars. We find that the data are reproduced by Pop III SNe with progenitor masses in the range [20–80] $M_\odot$ that experience strong fallback. For all the models we have identified the mass-coordinates that defines the extent of mixing and fallback that better reproduce the observed abundances, with particular attention on [C/Ca], [Mg/Ca] and [O/Ca] – that are extremely important for dust formation – without exceeding the upper limits on [Fe/Ca]. In the following, we discuss the properties of the faint Pop III SN progenitors inferred from the observed abundances of each star, which we also report in Table 9.

For *HE1327−2326*, nitrogen has been detected and the observed abundance shows comparable value of [N/Ca] and [C/Ca]. Since a substantial amount of N is produced only by Pop III SN models with progenitor masses in the range [25–35] $M_\odot$ (see Limongi & Chieffi 2012 for more details), we have limited the exploration of the mixing and fallback procedure to this mass range. The best agreement for HE1327–2326 is provided by the 30−$M_\odot$ progenitor model with a mass cut of 5 $M_\odot$ and an ejected mass of $M(^{56}\mathrm{Ni})$ of 3.68×10^{-7} $M_\odot$. Note that a [Si/Ca] ratio close to the observed upper limit implies a substantial underproduction of [(Na,Mg,Al)/Ca] ratios. Since the amount of Si in the ejecta plays a crucial role in the dust formation process, we chose to fit the [Si/Ca] ratio, even if the abundances of Na, Mg and Al are underproduced.

The same procedure has been applied to *HE0107−5240* finding the best agreement for a SN progenitor model with 35 $M_\odot$, a mass cut of 8 $M_\odot$ and an $M(^{56}\mathrm{Ni})$ mass of 9.12×10^{-7} $M_\odot$, which reproduces the observed [C/Ca] and [O/Ca] and predicts an [Na/Ca] ratio close to the observed one.

For *HE0557−4840* we have searched for progenitors which favour low [N/Ca] due to the low upper-limit inferred from observations. We select a 20 $M_\odot$ progenitor with $M_{\rm cut} = 5\,M_\odot$ and $M(^{56}\mathrm{Ni}) = 9.19 \times 10^{-7}$ $M_\odot$, that reproduces also the observed [C/Ca] and [Mg/Ca] abundances. We note that none of the models is able to reproduce, at the same time, the observed [O/Ca] and [Mg/Ca] abundances (see also Limongi & Chieffi 2012; Ishigaki et al. 2014), particularly the low-mass progenitors, which have lower value of [Mg/O] in the ejecta.

Finally, for *SMSS J031300* we have reported only the best fit obtained for the 80 $M_\odot$ model [$M_{\rm cut} = 24\,M_\odot$ and $M(^{56}\mathrm{Ni}) = 1.43 \times 10^{-7}$ $M_\odot$] selected by Marassi et al. (2014), to which we refer the reader for a detailed discussion.

6 DUST YIELDS FROM FAINT POP III SN

This section presents the results of the dust formation calculation for Pop III faint SN progenitors. To enable a comparison with the results by Marassi et al. (2014), we first discuss the results for uniformly mixed ejecta, which are presented in Table A7 in the appendix, where we give – for each of the four selected faint SN progenitors – the explosion parameters, the thermodynamical properties, the metal yields of the key elements in the nucleation process, the total amount of dust and the masses of molecules. Similarly to Marassi et al. (2014) we find that for all the progenitor models investigated, the only grain species that is able to condense and grow is AC. This is a consequence of the extensive fallback, which determine an ejecta composition dominated by carbon atoms, with an amount of Mg, Si

[3] In Marassi et al. (2014) we estimate that in less than 1 Myr the ejecta material can be well mixed and diluted with pristine gas, enriching the gas cloud out of which second-generation C-enhanced stars form with a [Fe/H] consistent with the observed values.

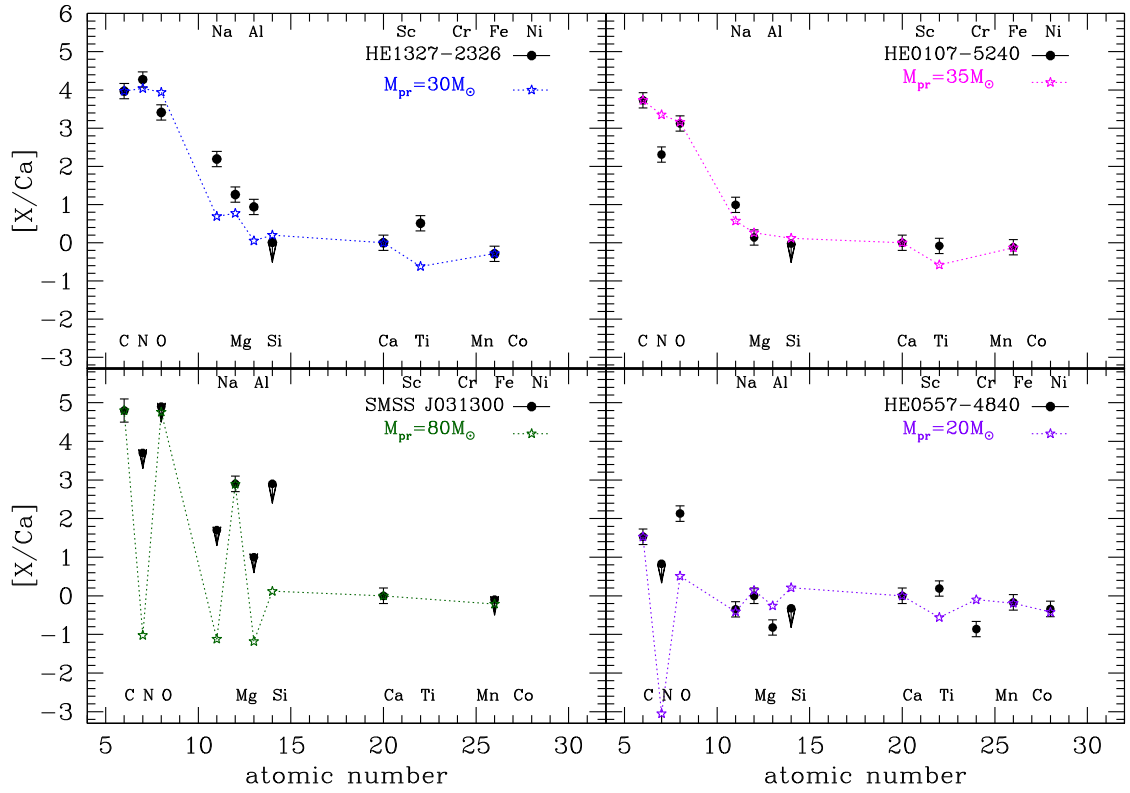

Figure 10. Comparison between the observed elemental abundance ratios of the CEMP-no stars and the chemical yields of Pop III faint SN with progenitor masses of 30, 35, 20, and 80 $M_{\odot}$. Mixing and fallback are chosen so as to minimize the scatter with the observations (black points). Dots with arrows show upper limits and filled points with error bars indicate the detections.

and Al which is too low to enable the condensation of other grain species (Marassi et al. 2014). We find that the molecular reactions involving SiO are negligible. The mass of AC is in the range $[2.7 \times 10^{-3}-0.269]\,M_{\odot}$, depending on the initial carbon abundance and on the mean ejecta density and temperature evolution. Due to the interplay of these quantities it is not possible to establish a direct correspondence between progenitor mass, ejected mass and the dust mass produced. As shown in Marassi et al. (2014), AC grains do not forms if the formation channels of carbon monoxide are efficient in subtracting carbon atoms from the ejecta, and this efficiency is greater when the mean ejecta density is larger. As a consequence, we note that HE0557–4840 have the greater condensation efficiency but the smaller AC mass is produced. Equally important is the temperature evolution which, in the case of HE0107–5240, enables the formation of C_2, subtracting C atoms from the ejecta.

In faint SNe, mixing occurs due to Rayleigh–Taylor instabilities up to a mass-coordinate that is very close to the mass cut (Umeda & Nomoto 2002); as a consequence, the material beyond the mass cut is likely to be stratified, and dust nucleation in unmixed ejecta gives a more reliable estimates of the total mass of dust produced. Table A8 shows the results for the unmixed ejecta model. For three of the four progenitor models, the stratified ejecta is composed of two layers A and B that have different average temperature, density and chemical composition. In particular, in all three unmixed models analysed, the internal layers A have mean ejecta density larger compared to the external layers B, enabling a very efficient formation of CO which inhibits the formation of AC.

The consequence of stratification is a reduction of the total mass of dust produced, that is in the range $[7.5 \times 10^{-4}-0.11]\,M_{\odot}$. In the left-hand panel of Fig. 11, we plot the total mass of dust before

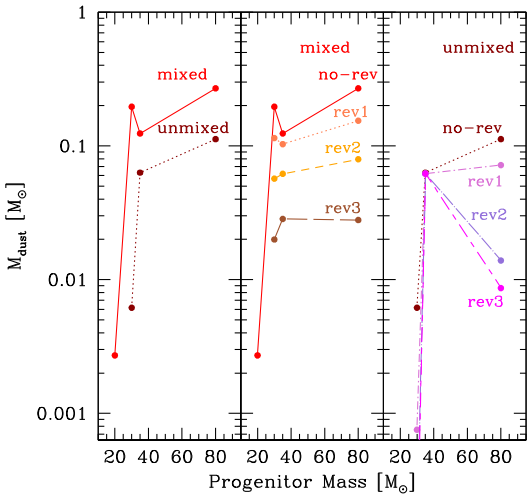

Figure 11. Left-hand panel: the mass of dust at the end of nucleation for mixed and unmixed ejecta for the four faint SN progenitors. Central panel: the mass of dust at the end of nucleation and after the passage of a reverse shock of increasing intensity for the four faint SN progenitors with mixed ejecta considered in this study. Right-hand panel: the same as in the central panel but for faint SN models with stratified ejecta. From top to bottom: no reverse shock models (no-rev), models with $n_{\rm ISM} = 0.06$ (rev1), 0.6 (rev2) and 6 $\rm cm^{-3}$ (rev3).

the passage of the reverse shock for mixed and unmixed models. Similarly to what has been done in Section 4, we have studied the impact of the reverse-shock on the above dust masses. The grain sizes originally follow a lognormal distribution in the range

[0.03–0.22] μm. As expected, after the passage of the shock the distribution flattens and shifts to lower grain sizes, due to the erosion of the larger grains caused by sputtering. In the central and right-hand panels of Fig. 11, we show the mass of dust that survives in uniformly mixed and stratified ejecta models, respectively. We find that, depending on the progenitor model, dust can be totally destroyed (as in the case of HE0557−4840) or that between 10 and 80 per cent of the original mass can survive. The passage of reverse shock in the unmixed case is less destructive than in the case of the fully mixed model. As discussed in Section 4, dust in external layers is highly affected by the reverse shock. On the contrary dust produced in internal layers, as in the case of HE0107 − 5240, is able to survive in large quantities, finding itself in milder conditions compared to the external layers.

7 CONCLUSIONS

In this study we have estimated the dust mass produced in the early Universe by Pop III *standard* and *faint* core-collapse SNe. For *standard* core-collapse events, which do not experience a strong fallback, the metal-free progenitors are calibrated to reproduce the average elemental abundances of Galactic halo stars with [Fe/H] < -2.5. We have enlarged our study to include Pop III faint SNe, which are fine-tuned to reproduce the abundance patterns observed on the surface of the sub-sample of carbon-enhanced hyper iron-poor stars.

To estimate the dust mass produced that survives the subsequent impact of the reverse shock, we have updated the previously developed code of Bianchi & Schneider (2007) to include formation/destruction processes of CO, SiO, C_2 and O_2 molecules that are crucial in subtracting gas-phase elements from the ejecta. We have investigated how our poor knowledge of mixing can affect the resulting dust yields by analysing both uniformly mixed and stratified ejecta. Finally, to have a more realistic estimate of the dust mass that will be injected into the ISM, we have analysed the effect of the passage of the reverse-shock. Our main results are as follows.

(i) Standard core-collapse Pop III SNe are efficient dust producers when the ejecta are uniformly mixed; the newly formed dust mass is in the range [0.18–3] $M_\odot$ and is dominated by silicates. Depending on the density of the ISM, the impact of the reverse shock on the newly formed dust is to reduce the original dust mass by a factor which ranges between 3 and 48 per cent, changing the relative abundance of different dust species. The mass of dust produced depends on the degree of mixing experienced by the ejecta. In general, silicates, magnetites and alumina grains are formed in the internal layers, while AC forms only in the external layers that are carbon and oxygen dominated. In stratified ejecta dust does not form at the same time in each layer, with silicates forming in the inner layers before AC in the external ones. For the same SN progenitor model, the mass of dust formed in unmixed ejecta can be smaller or higher than in the corresponding mixed case, with variations which amount to 3–10 per cent.

(ii) We confirm the results found by Marassi et al. (2014) that dust can form in the ejecta of faint Pop III SNe. As a consequence of the larger fallback experienced with respect to standard core-collapse Pop III SNe, the ejecta is lacking in silicate, magnesium and alumina and the only dust grain that forms is AC. The total amount of carbon dust produced in the uniformly mixed case varies in the range [0.2–0.27] $M_\odot$, and in the stratified case in the range [7.4×10^{-4}–0.11] $M_\odot$ depending on the model. After the passage of the reverse shock, the dust that survives ranges between 10 and 80 per cent.

The mass and composition of dust formed in the ejecta of Pop III SNe depends on the degree of fallback. In *standard* Pop III SNe, the mass-cut corresponds to a mass coordinate in the range [1.48–2.44] $M_\odot$. As a result, almost all the mantle is ejected with a greater amount of internal elements, such as silicon and magnesium, favouring the condensation of silicates. The observed elemental abundances of CEMP stars with [Fe/H] < -4 require Pop III SN progenitors with masses in the range [20–80] $M_\odot$ which experience a strong fallback, with mass cut which corresponds to mass coordinates in the range [5–24] $M_\odot$. These *faint* SNe leave a much larger remnant behind and eject a smaller amount of metals, with mantles dominated by light elements. These properties of the SNe largely affect the mass and composition of dust which condense in the ejecta, as shown by Fig. 12, where we summarize our results showing the mass of metals and of the dominant grain species produced by *standard (left-hand panel)* and *faint (right-hand panel)* Pop III SNe. Note that for each SN model, we have rescaled the mass of metals and dust as $M^*_{\rm met} = M_{\rm eje} M_{\rm met}/(M_{\rm met} + M_{\rm dust})$ and $M^*_{\rm dust} = M_{\rm eje} M_{\rm dust}/(M_{\rm met} + M_{\rm dust})$, to clearly display these

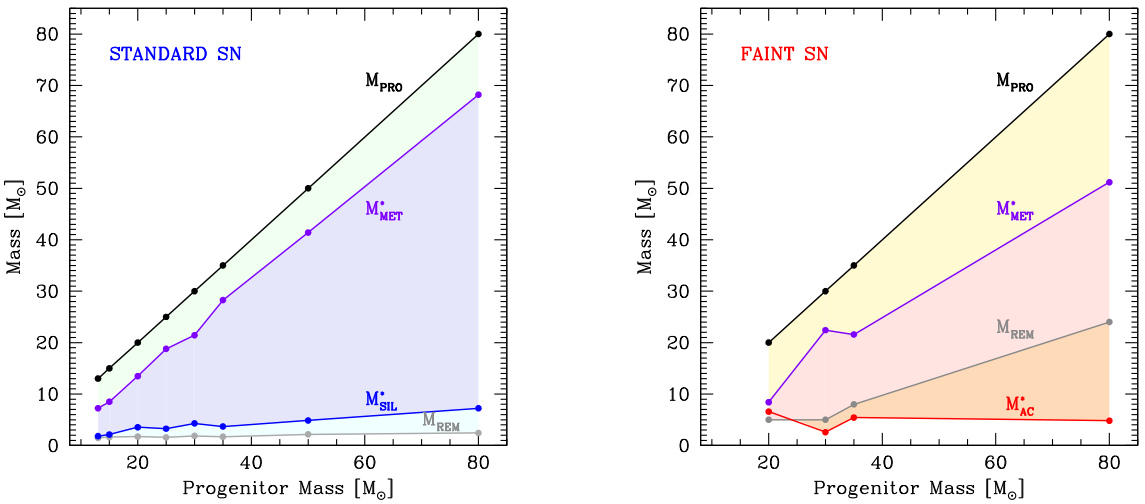

Figure 12. Mass of the SN progenitor, of the remnant, of metals and dust mass as a function of the progenitor mass for standard (left-hand panel) and faint (right-hand panel) Pop III SNe. Note that the mass of metals and dust have been multiplied by $M_{\rm eje}/(M_{\rm met} + M_{\rm dust})$ (see text).

physical quantities. Finally we have constructed, starting from our set of metal-free progenitors, a dust data grid for Pop III SNe which provides the initial conditions required to simulate the properties of the first metal-enriched star-forming regions at high redshift. In addition, we plan to extend this analysis to higher metallicity to incorporate these new mass- and metallicity-dependent yields in chemical evolution models with dust.

ACKNOWLEDGEMENTS

We thank the anonymous referee for her/his careful reading of the manuscript and useful comments. The research leading to these results has received funding from the European Research Council under the European Union's Seventh Framework Programme (FP/2007-2013)/ERC Grant Agreement no. 306476. We acknowledge financial support from PRIN MIUR 2010-2011, project 'The Chemical and dynamical Evolution of the Milky Way and Local Group Galaxies', prot. 2010LY5N2T.

REFERENCES

Andreazza C. M., Singh P. D., 1997, MNRAS, 287, 287
Asplund M., Grevesse N., Sauval A. J., Scott P., 2009, ARA&A, 47, 48
Babb J. F., Dalgarno A., 1995, Phys. Rev. A, 51, 3021
Barlow M. J. et al., 2010, A&A, 518, 138
Beers T. C., Christlieb N., 2005, ARA&A, 43, 531
Bianchi S., Schneider R., 2007, MNRAS, 378, 973
Cherchneff I., Dwek E., 2009, ApJ, 703, 642
Cherchneff I., Dwek E., 2010, ApJ, 713, 1
Chieffi A., Limongi M., 2002, ApJ, 577, 281
Christlieb N. et al., 2002, Nature, 419, 904
Dalgarno A., Du M. L., You J. H., 1990, ApJ, 349, 675
de Bennassuti M., Schneider R., Valiante R., Salvadori S., 2014, MNRAS, 445, 3039
Donn B., Nuth J. A., 1985, ApJ, 288, 187
Frebel A. et al., 2005, Nature, 434, 871
Heger A., Woosley S. E., 2010, ApJ, 724, 341
Hirano S., Hosokawa T., Yoshida N., Umeda H., Omukai K., Chiaki G., Yorke H. W., 2014, ApJ, 781, 60
Hirano S., Hosokawa T., Yoshida N., Omukai K., Yorke H. W., 2015, MNRAS, 448, 568
Hirashita H., Omukai K., 2009, MNRAS, 399, 1795
Hosokawa T., Omukai K., Yoshida N., Yorke H. W., 2011, Science, 334, 1250
Hosokawa T., Yoshida N., Omukai K., Yorke H. W., 2012, ApJ, 760, 37
Indebetouw R. et al., 2014, ApJ, 782, 2
Ishigaki M., Tominaga N., Kobayashi C., Nomoto K., 2014, ApJL, 792, 32
Iwamoto N., Umeda H., Tominaga N., Nomoto K., Maeda K., 2005, Science, 309, 451
Joggerst C. C., Woosley S. E., Heger A., 2009, ApJ, 693, 1780
Keller S. C. et al., 2014, Nature, 506, 463
Kochanek C. S., 2014, MNRAS, 444, 2043
Kozasa T., Hasegawa H., Nomoto K., 1989, ApJ, 344, 325
Kozasa T., Hasegawa H., Nomoto K., 1991, A&A, 249, 474
Limongi M., Chieffi A., 2006, ApJ, 647, 483
Limongi M., Chieffi A., 2012, ApJS, 199, 38
Limongi M., Chieffi A., Bonifacio P., 2003, ApJ, 594, 123
Maeder A., Meynet G., Chiappini C., 2015, A&A, 576, A56
Marassi S., Chiaki G., Schneider R., Limongi M., Omukai K., Nozawa T., Chieffi A., Yoshida N., 2014, ApJ, 794, 100
Matsuura M. et al., 2011, Science, 333, 1258
Norris J. E., Christlieb N., Korn A. J., Eriksson K., Bessell M. S., Beers T. C., Wisotzki L., Reimers D., 2007, ApJ, 670, 774
Norris J. E. et al., 2013, ApJ, 762, 28
Nozawa T., Kozasa T., 2003, ApJ, 598, 785
Nozawa T., Kozasa T., 2013, ApJ, 776, 24
Nozawa T., Kozasa T., Umeda H., Maeda K., Nomoto K., 2003, ApJ, 598, 785
Nozawa T., Kozasa T., Habe A., Dwek E., Umeda H., Tominaga N., Maeda K., Nomoto K., 2007, ApJ, 666, 955
Nozawa T. et al., 2008, ApJ, 684, 1343
Nozawa T., Kozasa T., Tominaga N., Maeda K., Umeda H., Nomoto K., Krause O., 2010, ApJ, 713, 356
Nozawa T., Maeda K., Kozasa T., Tanaka M., Nomoto K., Umeda H., 2011, ApJ, 736, 45
Paquette J. A., Nuth J. A., III, 2011, ApJ, 737, 6
Placco V. M., Frebel A., Beers T. C., Stancliffe R. J., 2014, ApJ, 797, 21
Sarangi A., Cherchneff I., 2013, ApJ, 776, 107
Sarangi A., Cherchneff I., 2015, A&A, 575, 95
Schneider R., Omukai K., 2010, MNRAS, 402, 429
Schneider R., Salvaterra R., Ferrara A., 2004, MNRAS, 351, 1379
Schneider R., Omukai K., Limongi M., Ferrara A., Salvaterra R., Chieffi A., Bianchi S., 2012, MNRAS, 423, L60
Schneider R., Valiante R., Ventura P., dell'Agli F., Di Criscienzo M., Hirashita H., Kemper F., 2014, MNRAS, 442, 1440
Silvia D. W., Smith B. D., Shull J. M., 2010, ApJ, 715, 1575
Silvia D. W., Smith B. D., Shull J. M., 2012, ApJ, 748, 12
Susa H., Hasegawa K., Tominaga N., 2014, ApJ, 792, 32
Todini P., Ferrara A., 2001, MNRAS, 325, 726
Tominaga N., 2009, ApJ, 690, 526
Tominaga N., Umeda H., Nomoto K., 2007, ApJ, 660, 516
Tominaga N., Iwamoto N., Nomoto K., 2014, ApJ, 785, 98
Truelove J. K., McKee C. F., 1999, ApJ, 120, 299
Umeda H., Nomoto K., 2002, ApJ, 565, 385
Umeda H., Nomoto K., 2003, Nature, 422, 871
Valiante R., Schneider R., 2014, Proc. Sci., Dust in the first quasars as a powerful probe of galaxy/BH co-evolution. SISSA, Treiste, PoS(LCDU2013)012
Woosley S. E., Pinto P. A., Hartmann D., 1989, ApJ, 346, 395
Yong D. et al., 2013, ApJ, 762, 26

APPENDIX A: FINAL DUST GRIDS AND TABLES

In this appendix we report all the useful tables: for all progenitors we report chemical composition (yields), mass of molecules, mass of dust etc.

Table A1. Properties of the Pop III SNe, including the explosion energy (10^{51} erg), the ejecta velocity (km s^{-1}), the mass of the ejecta, the mass cut and the mass of the helium core ($M_\odot$), the gas number density (cm^{-3}) and the radius of He core, R_0 (cm) at $t = t_{ini}$ (s) when adiabatic expansion starts (see text); the initial masses of C, O, Mg, Si, Al, Fe and ^{56}Ni which decays in ^{56}Co fuelling γ-luminosity (see equation 2), the mass of molecules, CO, SiO, O_2, C_2 and the grains formed in the expanding ejecta ($M_\odot$). Each model name identifies the progenitor mass.

Pop III SN – fully mixed ejecta models								
	13 $M_\odot$	15 $M_\odot$	20 $M_\odot$	25 $M_\odot$	30 $M_\odot$	35 $M_\odot$	50 $M_\odot$	80 $M_\odot$
E_{exp}	0.5	0.7	1.0	1.1	1.6	1.3	2.6	5.2
v_{eje}	2696	2960	3027	2805	3086	2557	3017	3351
M_{eje}	11.52	13.38	18.28	23.42	28.14	33.30	47.84	77.55
M_{cut}	1.48	1.62	1.72	1.58	1.86	1.70	2.16	2.44
$M_{He_{core}}$	2.81	3.40	5.18	5.37	7.22	11.13	18.11	31.94
R_0	2.65×10^{14}	2.44×10^{14}	1.47×10^{14}	3.75×10^{14}	4.68×10^{14}	1.98×10^{14}	2.51×10^{14}	4.78×10^{14}
t_{ini}	2.11×10^{6}	1.78×10^{6}	1.58×10^{6}	3.72×10^{6}	3.96×10^{6}	3.11×10^{6}	3.12×10^{6}	4.14×10^{6}
n_0	2.71×10^{11}	7.18×10^{11}	8.34×10^{12}	9.31×10^{11}	7.39×10^{11}	1.26×10^{13}	1.24×10^{13}	3.65×10^{12}
$M(^{56}Ni)$	2.20×10^{-2}	3.85×10^{-2}	7.12×10^{-2}	9.54×10^{-2}	2.10×10^{-1}	1.81×10^{-1}	2.86×10^{-1}	4.86×10^{-1}
M_C	7.52×10^{-2}	1.56×10^{-1}	2.99×10^{-1}	4.48×10^{-1}	7.02×10^{-1}	6.21×10^{-1}	1.44	2.43
M_O	1.38×10^{-1}	2.91×10^{-1}	9.31×10^{-1}	1.96	2.96	4.35	8.60	18.22
M_{Mg}	1.83×10^{-2}	3.61×10^{-2}	9.99×10^{-2}	9.34×10^{-2}	1.33×10^{-2}	2.15×10^{-1}	2.03×10^{-1}	3.66×10^{-1}
M_{Si}	4.42×10^{-2}	8.49×10^{-2}	1.12×10^{-1}	1.59×10^{-1}	3.23×10^{-1}	1.72×10^{-1}	4.46×10^{-1}	8.22×10^{-1}
M_{Al}	6.63×10^{-4}	1.42×10^{-3}	3.11×10^{-3}	2.50×10^{-3}	2.31×10^{-3}	3.49×10^{-3}	1.85×10^{-3}	3.61×10^{-3}
M_{Fe}	2.31×10^{-2}	4.03×10^{-2}	7.39×10^{-2}	1.00×10^{-1}	2.18×10^{-1}	1.87×10^{-1}	2.95×10^{-1}	5.04×10^{-1}
M_{CO}	9.60×10^{-3}	3.43×10^{-2}	0.65	0.896	1.25	1.45	3.36	5.66
M_{SiO}	–	–	–	–	–	–	–	–
M_{O_2}	–	–	–	–	–	0.77	1.41	1.64
M_{C_2}	–	–	–	–	–	–	–	–
M_{AC}	7.10×10^{-2}	0.14	1.80×10^{-2}	6.36×10^{-2}	0.16	–	–	–
M_{MgSiO_3}	2.17×10^{-4}	5.10×10^{-5}	–	3.86×10^{-4}	5.62×10^{-3}	–	3.23×10^{-6}	5.76×10^{-4}
$M_{Mg_2SiO_4}$	5.28×10^{-2}	0.104	0.29	0.27	0.38	0.62	0.59	1.06
$M_{Fe_3O_4}$	3.00×10^{-2}	5.65×10^{-2}	0.11	0.14	0.30	0.263	0.41	0.70
M_{SiO_2}	2.12×10^{-2}	4.93×10^{-2}	0.11	0.21	0.46	0.102	0.70	1.31
$M_{Al_2O_3}$	1.25×10^{-3}	2.67×10^{-3}	5.88×10^{-3}	4.72×10^{-3}	4.36×10^{-3}	6.60×10^{-3}	3.50×10^{-3}	6.83×10^{-3}
M_{dust}	0.176	0.35	0.54	0.68	1.32	0.99	1.71	3.07

Table A2. Properties of the 15-$M_\odot$ Pop III SN unmixed ejecta model. In unmixed models R_0 and n_0 are the mean radius and density of the layers.

15-$M_\odot$ unmixed ejecta model			
E_{exp} =0.7	$M_{He_{core}} = 3.40$	$v_{eje} = 2960$	$M_{eje} = 13.38$
	Zone A (1.62–1.98) $M_\odot$	Zone B (1.98–2.22) $M_\odot$	Zone C (2.22–3.40) $M_\odot$
R_0	3.50×10^{14}	1.96×10^{14}	2.22×10^{14}
t_{ini}	3.19×10^{5}	1.77×10^{6}	1.78×10^{6}
n_0	7.18×10^{12}	7.50×10^{12}	2.37×10^{11}
$M(^{56}Ni)$	3.85×10^{-2}	–	–
M_C	1.88×10^{-3}	9.48×10^{-2}	5.95×10^{-2}
M_O	0.17	0.12	7.50×10^{-3}
M_{Mg}	3.52×10^{-2}	8.87×10^{-4}	–
M_{Si}	8.45×10^{-2}	3.60×10^{-4}	–
M_{Al}	1.38×10^{-3}	3.36×10^{-5}	–
M_{Fe}	4.04×10^{-2}	–	–
M_{CO}	4.38×10^{-3}	0.18	1.32×10^{-2}
M_{SiO}	–	–	–
M_{O_2}	3.00×10^{-2}	–	–
M_{C_2}	–	–	1.34×10^{-2}
M_{AC}	–	1.69×10^{-2}	4.03×10^{-2}
M_{MgSiO_3}	–	–	–
$M_{Mg_2SiO_4}$	0.10	1.77×10^{-3}	–
$M_{Fe_3O_4}$	7.46×10^{-2}	–	–
M_{SiO_2}	0.14	–	–
$M_{Al_2O_3}$	2.61×10^{-3}	6.36×10^{-5}	–
M_{Fe}	1.25×10^{-2}	–	–
M_{dust}	0.33	1.88×10^{-2}	4.03×10^{-2}

Table A3. Properties of the 30-$M_\odot$ Pop III SN unmixed ejecta model.

30-$M_\odot$ unmixed ejecta model			
E_{exp} =1.6	$M_{He_{core}} = 7.22$	$v_{eje} = 3086$	$M_{eje} = 28.14$
	Zone A (1.86–3.99) $M_\odot$	Zone B (3.99–5.20) $M_\odot$	Zone C (5.20–7.22) $M_\odot$
R_0	3.29×10^{14}	3.63×10^{14}	4.52×10^{14}
t_{ini}	3.13×10^{6}	3.28×10^{6}	3.96×10^{6}
n_0	1.97×10^{12}	1.37×10^{13}	1.50×10^{12}
$M(^{56}Ni)$	2.10×10^{-1}	–	–
M_C	1.26×10^{-2}	0.23	0.45
M_O	0.75	1.19	1.00
M_{Mg}	9.91×10^{-2}	3.39×10^{-2}	1.94×10^{-5}
M_{Si}	0.32	1.59×10^{-3}	–
M_{Al}	1.65×10^{-3}	6.60×10^{-4}	–
M_{Fe}	0.22	–	–
M_{CO}	2.95×10^{-2}	0.53	1.04
M_{SiO}	–	–	–
M_{O_2}	1.97×10^{-3}	0.46	–
M_{C_2}	–	–	–
M_{AC}	–	–	9.32×10^{-3}
M_{MgSiO_3}	–	–	–
$M_{Mg_2SiO_4}$	0.29	7.96×10^{-3}	–
$M_{Fe_3O_4}$	0.30	–	–
M_{SiO_2}	0.56	–	–
$M_{Al_2O_3}$	3.11×10^{-3}	1.25×10^{-3}	–
M_{Fe}	–	–	–
M_{dust}	1.15	9.21×10^{-3}	9.32×10^{-3}

Table A4. Properties of the 50-$M_\odot$ Pop III SN unmixed ejecta model.

50-$M_\odot$ unmixed ejecta model			
E_{exp} =2.6	$M_{He_{core}} = 18.11$	$v_{eje} = 3017$	$M_{eje} = 47.84$
	Zone A (2.16–4.31) $M_\odot$	Zone B (4.31–11.51) $M_\odot$	Zone C (11.51–18.11) $M_\odot$
R_0	2.16×10^{13}	3.45×10^{13}	1.11×10^{14}
t_{ini}	4.76×10^{5}	6.75×10^{5}	3.12×10^{6}
n_0	1.47×10^{14}	1.24×10^{14}	6.60×10^{12}
$M(^{56}Ni)$	2.86×10^{-1}	–	–
M_C	2.76×10^{-3}	0.56	0.87
M_O	1.05	5.49	2.05
M_{Mg}	9.56×10^{2}	0.106	6.60×10^{-4}
M_{Si}	0.44	5.40×10^{-3}	–
M_{Al}	–	8.3×10^{-4}	–
M_{Fe}	0.29	–	–
M_{CO}	6.44×10^{-3}	1.31	1.76
M_{SiO}	–	–	–
M_{O_2}	0.46	3.46	1.38×10^{-3}
M_{C_2}	–	–	–
M_{AC}	–	–	0.12
M_{MgSiO_3}	2.42×10^{-2}	–	–
$M_{Mg_2SiO_4}$	0.26	2.71×10^{-2}	–
$M_{Fe_3O_4}$	0.20	–	–
M_{SiO_2}	0.82	–	–
$M_{Al_2O_3}$	–	1.58×10^{-3}	–
M_{Fe}	0.31	–	–
M_{dust}	1.61	2.87×10^{-2}	0.12

Table A5. The total mass of dust and of each grain species after the passage of the reverse shock of increasing strength for all Pop III SN ejecta models.

Pop III SN – reverse shock – fully mixed ejecta models								
				rev1				
	13 $M_\odot$	15 $M_\odot$	20 $M_\odot$	25 $M_\odot$	30 $M_\odot$	35 $M_\odot$	50 $M_\odot$	80 $M_\odot$
M_{AC}	4.78×10^{-2}	9.82×10^{-2}	6.71×10^{-3}	3.59×10^{-2}	0.10	–	–	–
M_{MgSiO_3}	3.45×10^{-5}	1.19×10^{-5}	–	1.20×10^{-4}	1.58×10^{-3}	–	1.44×10^{-6}	1.68×10^{-4}
$M_{Mg_2SiO_4}$	7.72×10^{-3}	2.13×10^{-2}	0.17	7.45×10^{-2}	9.41×10^{-2}	0.39	0.24	0.27
$M_{Fe_3O_4}$	1.25×10^{-3}	3.49×10^{-3}	2.35×10^{-2}	1.21×10^{-2}	2.85×10^{-2}	5.54×10^{-2}	7.06×10^{-2}	5.77×10^{-2}
M_{SiO_2}	2.22×10^{-3}	8.59×10^{-3}	4.76×10^{-2}	6.33×10^{-2}	0.15	3.37×10^{-2}	0.37	0.47
$M_{Al_2O_3}$	7.29×10^{-5}	1.34×10^{-4}	6.82×10^{-4}	2.75×10^{-4}	2.89×10^{-4}	6.33×10^{-4}	1.52×10^{-4}	2.24×10^{-4}
M_{dust}	5.9×10^{-2}	0.13	0.25	0.19	0.38	0.48	0.68	0.80
				rev2				
	13 $M_\odot$	15 $M_\odot$	20 $M_\odot$	25 $M_\odot$	30 $M_\odot$	35 $M_\odot$	50 $M_\odot$	80 $M_\odot$
M_{AC}	2.43×10^{-2}	5.53×10^{-2}	2.83×10^{-3}	1.71×10^{-2}	5.31×10^{-2}	–	–	–
M_{MgSiO_3}	1.11×10^{-5}	3.86×10^{-6}	–	4.18×10^{-5}	5.30×10^{-4}	–	5.68×10^{-7}	5.55×10^{-5}
$M_{Mg_2SiO_4}$	2.48×10^{-3}	6.76×10^{-3}	7.82×10^{-2}	2.49×10^{-2}	3.01×10^{-2}	0.16	8.96×10^{-2}	8.66×10^{-2}
$M_{Fe_3O_4}$	5.36×10^{-4}	1.13×10^{-3}	7.07×10^{-3}	3.58×10^{-3}	8.07×10^{-3}	1.63×10^{-2}	1.98×10^{-2}	1.43×10^{-2}
M_{SiO_2}	7.72×10^{-4}	2.72×10^{-3}	1.87×10^{-2}	2.22×10^{-2}	5.61×10^{-2}	1.17×10^{-2}	0.16	0.17
$M_{Al_2O_3}$	3.73×10^{-5}	6.66×10^{-5}	2.30×10^{-4}	1.25×10^{-4}	1.06×10^{-4}	2.32×10^{-4}	7.13×10^{-5}	1.11×10^{-4}
M_{dust}	2.8×10^{-2}	6.6×10^{-2}	0.11	6.8×10^{-2}	0.15	0.19	0.27	0.27
				rev3				
	13 $M_\odot$	15 $M_\odot$	20 $M_\odot$	25 $M_\odot$	30 $M_\odot$	35 $M_\odot$	50 $M_\odot$	80 $M_\odot$
M_{AC}	9.27×10^{-3}	2.40×10^{-2}	9.16×10^{-4}	5.80×10^{-3}	1.95×10^{-2}	–	–	–
M_{MgSiO_3}	5.11×10^{-6}	1.34×10^{-6}	–	1.28×10^{-5}	1.59×10^{-4}	–	–	1.67×10^{-5}
$M_{Mg_2SiO_4}$	1.17×10^{-3}	2.39×10^{-3}	2.67×10^{-2}	7.62×10^{-3}	9.55×10^{-3}	5.50×10^{-2}	2.62×10^{-2}	2.69×10^{-2}
$M_{Fe_3O_4}$	4.17×10^{-4}	7.37×10^{-4}	2.32×10^{-3}	1.81×10^{-3}	2.80×10^{-3}	5.45×10^{-3}	6.43×10^{-3}	5.91×10^{-3}
M_{SiO_2}	4.57×10^{-4}	1.11×10^{-3}	5.97×10^{-3}	7.02×10^{-3}	1.65×10^{-2}	3.87×10^{-3}	5.05×10^{-2}	4.97×10^{-2}
$M_{Al_2O_3}$	2.80×10^{-5}	5.11×10^{-5}	1.29×10^{-4}	8.39×10^{-5}	6.69×10^{-5}	1.52×10^{-4}	5.26×10^{-5}	1.03×10^{-4}
M_{dust}	1.1×10^{-2}	2.8×10^{-2}	3.6×10^{-2}	2.2×10^{-2}	4.9×10^{-2}	6.4×10^{-2}	8.3×10^{-2}	8.3×10^{-2}

Table A6. The total mass of dust and of each grain species after the passage of the reverse shock of increasing strength for selected unmixed Pop III SN ejecta models.

Pop III SN – reverse shock – unmixed ejecta models									
					rev1				
	15 $M_\odot$ A	15 $M_\odot$ B	15 $M_\odot$ C	30 $M_\odot$ A	30 $M_\odot$ B	30 $M_\odot$ C	50 $M_\odot$ A	50 $M_\odot$ B	50 $M_\odot$ C
M_{AC}	–	1.19×10^{-2}	3.47×10^{-2}	–	–	3.06×10^{-3}	–	–	1.19×10^{-1}
M_{MgSiO_3}	–	–	–	–	–	–	2.42×10^{-2}	–	–
$M_{Mg_2SiO_4}$	0.10	–	–	0.21	2.05×10^{-5}	–	0.26	1.96×10^{-2}	–
$M_{Fe_3O_4}$	7.45×10^{-2}	–	–	0.13	–	–	0.20	–	–
M_{SiO_2}	0.12	–	–	0.56	–	–	0.82	–	–
$M_{Al_2O_3}$	1.27×10^{-3}	–	–	–	–	–	–	4.13×10^{-4}	–
M_{Fe}	1.20×10^{-2}	–	–	–	–	–	0.31	–	–
M_{dust}	3.16×10^{-1}	1.19×10^{-2}	3.47×10^{-2}	8.94×10^{-1}	2.05×10^{-5}	3.06×10^{-3}	1.61	2.0×10^{-2}	1.19×10^{-1}
					rev2				
	15 $M_\odot$ A	15 $M_\odot$ B	15 $M_\odot$ C	30 $M_\odot$ A	30 $M_\odot$ B	30 $M_\odot$ C	50 $M_\odot$ A	50 $M_\odot$ B	50 $M_\odot$ C
M_{AC}	–	1.19×10^{-2}	1.35×10^{-2}	–	–	1.11×10^{-3}	–	–	7.02×10^{-2}
M_{MgSiO_3}	–	–	–	–	–	–	2.42×10^{-2}	–	–
$M_{Mg_2SiO_4}$	9.53×10^{-2}	–	–	3.79×10^{-2}	–	–	0.26	6.37×10^{-3}	–
$M_{Fe_3O_4}$	4.69×10^{-2}	–	–	4.84×10^{-4}	–	–	0.20	–	–
M_{SiO_2}	7.22×10^{-2}	–	–	0.30	–	–	0.82	–	–
$M_{Al_2O_3}$	1.01×10^{-5}	–	–	–	–	–	–	4.50×10^{-5}	–
M_{Fe}	4.24×10^{-3}	–	–	–	–	–	0.31	–	–
M_{dust}	2.19×10^{-1}	1.19×10^{-2}	1.35×10^{-2}	3.37×10^{-1}	–	1.11×10^{-3}	1.61	6.42×10^{-3}	7.02×10^{-2}

Table A6 – *continued*

Pop III SN – reverse shock – unmixed ejecta models									
				rev3					
	$15M_\odot$	$15\,M_\odot$	$15\,M_\odot$	$30\,M_\odot$	$30\,M_\odot$	$30\,M_\odot$	$50\,M_\odot$	$50\,M_\odot$	$50\,M_\odot$
	A	B	C	A	B	C	A	B	C
M_{AC}	–	3.84×10^{-3}	2.77×10^{-3}	–	–	9.08×10^{-4}	–	–	1.61×10^{-2}
M_{MgSiO_3}	–	–	–	–	–	–	2.42×10^{-2}	–	–
$M_{Mg_2SiO_4}$	3.12×10^{-2}	–	–	–	–	–	0.26	6.53×10^{-4}	–
$M_{Fe_3O_4}$	4.17×10^{-3}	–	–	–	–	–	0.20	–	–
M_{SiO_2}	8.36×10^{-3}	–	–	1.26×10^{-2}	–	–	0.81	–	–
$M_{Al_2O_3}$	–	–	–	–	–	–	–	–	–
M_{Fe}	1.74×10^{-5}	–	–	–	–	–	0.31	–	–
M_{dust}	4.38×10^{-2}	3.84×10^{-3}	2.77×10^{-3}	1.26×10^{-2}	–	9.08×10^{-4}	1.61	6.53×10^{-4}	1.61×10^{-2}

Table A7. Properties of the faint Pop III SN progenitors, including [Fe/H], the explosion energy (10^{51} erg), the mass of the helium core, the ejecta velocity (km s^{-1}), the mass of the ejecta, the gas number density (cm^{-3}) and the radius of He core, R_0 (cm) at $t = t_{ini}$ (s) when adiabatic expansion starts (see text); the initial masses of C, O, Mg, Si, Al and Fe, and the mass of molecules, CO, SiO, O_2, C_2 and the grains formed in the expanding ejecta ($M_\odot$).

Pop III faint SN – fully mixed ejecta models				
	HE1327−2326	HE0107−5240	HE0557−4840	SMSSJ031300
[Fe/H]	−5.76	−5.54	−4.81	−7.1
	$30\,M_\odot$	$35\,M_\odot$	$20\,M_\odot$	$80\,M_\odot$
E_{exp}	1.6	1.3	1.0	5.2
$M_{He_{core}}$	7.22	11.13	5.18	31.94
v_{eje}	3273	2833	3301	3943
M_{eje}	25	27	15	56
M_{cut}	5	8	5	24
R_0	4.68×10^{14}	1.98×10^{14}	1.47×10^{14}	4.78×10^{14}
t_{ini}	3.96×10^{6}	3.11×10^{6}	1.58×10^{6}	4.14×10^{6}
n_0	3.27×10^{11}	1.36×10^{12}	2.46×10^{10}	5.17×10^{11}
$M(^{56}Ni)$	3.68×10^{-7}	9.12×10^{-7}	9.19×10^{-7}	1.43×10^{-7}
M_C	0.51	0.297	2.76×10^{-3}	0.887
M_O	1.19	0.195	6.37×10^{-4}	1.973
M_{Mg}	9.74×10^{-5}	3.02×10^{-5}	3.37×10^{-5}	3.26×10^{-3}
M_{Si}	2.81×10^{-5}	2.07×10^{-5}	3.78×10^{-5}	5.19×10^{-6}
M_{Ca}	1.50×10^{-6}	1.50×10^{-6}	2.21×10^{-6}	3.82×10^{-7}
M_{Fe}	1.58×10^{-5}	2.24×10^{-6}	2.82×10^{-5}	4.7×10^{-6}
M_{CO}	0.74	0.342	1.12×10^{-4}	1.44
M_{SiO}	4.0×10^{-5}	2.7×10^{-5}	1.8×10^{-7}	3.5×10^{-6}
M_{O_2}	1.2×10^{-5}	–	–	2.4×10^{-5}
M_{C_2}	–	2.6×10^{-2}	–	–
M_{AC}	0.196	0.124	2.71×10^{-3}	0.269

Table A8. Properties of the faint Pop III SN unmixed models, including the explosion energy (10^{51} erg), the mass of the ejecta, the initial masses of C, O, Mg, Si, Al and Fe, and the mass of CO and the grains formed in the expanding ejecta ($M_\odot$). Each model name identifies the progenitor mass.

Pop III faint SN – unmixed ejecta models						
	HE1327−2326	HE1327−2326	HE0107−5240	HE0107−5240	SMSSJ031300	SMSSJ031300
	30 $M_\odot$	30 $M_\odot$	35 $M_\odot$	35 $M_\odot$	80 $M_\odot$	80 $M_\odot$
	A	B	A	B	A	B
E_{exp}	1.6	1.6	1.3	1.3	5.2	5.2
M_{eje}	25	25	27	27	56	56
v_{eje}	3273	3273	2833	2833	3943	3943
M_{cut}	5	5	8	8	24	24
R_0	2.18×10^{14}	4.73×10^{14}	1.45×10^{14}	2.21×10^{14}	2.29×10^{14}	4.57×10^{14}
t_{ini}	1.90×10^{6}	2.45×10^{6}	2.66×10^{6}	1.84×10^{6}	2.24×10^{6}	4.14×10^{6}
n_0	1.76×10^{13}	2.4×10^{9}	1.98×10^{12}	2.96×10^{9}	2.33×10^{13}	3.31×10^{11}
$M(^{56}Ni)$	3.68×10^{-7}	–	9.12×10^{-7}	–	1.43×10^{-7}	–
M_C	0.508	6.35×10^{-3}	0.296	7.61×10^{-4}	0.547	0.339
M_O	1.162	2.60×10^{-2}	0.192	3.77×10^{-3}	1.948	0.024
M_{Mg}	9.74×10^{-5}	–	3.00×10^{-5}	–	3.26×10^{-3}	–
M_{Si}	2.81×10^{-5}	–	2.06×10^{-5}	–	5.19×10^{-6}	–
M_{Ca}	1.50×10^{-6}	–	1.50×10^{-6}	–	3.82×10^{-7}	–
M_{Fe}	1.58×10^{-5}	–	2.23×10^{-5}	–	4.7×10^{-6}	–
M_{CO}	1.18	3.80×10^{-4}	0.33	3.21×10^{-5}	1.276	0.043
M_{SiO}	–	–	–	–	–	–
M_{O_2}	0.11	–	–	–	0.513	–
M_{C_2}	–	–	9.05×10^{-2}	–	–	0.21
M_{AC}	–	6.18×10^{-3}	6.21×10^{-2}	7.47×10^{-4}	–	0.112

Table A9. The total mass of dust after the passage of the reverse shock of increasing strength for all faint Pop III SN ejecta models.

Pop III faint SN – reverse shock – fully mixed ejecta models				
	HE1327−2326	HE0107−5240	HE0557−4840	SMSSJ031300
	30 $M_\odot$	35 $M_\odot$	20 $M_\odot$	80 $M_\odot$
		rev1		
M_{AC}	0.11	0.10	8.3×10^{-4}	0.15
		rev2		
M_{AC}	5.7×10^{-2}	6.2×10^{-2}	3.0×10^{-4}	7.8×10^{-2}
		rev3		
M_{AC}	1.99×10^{-2}	2.8×10^{-2}	9.0×10^{-5}	2.8×10^{-2}

Table A10. The total mass of dust after the passage of the reverse shock of increasing strength for selected unmixed faint Pop III SN ejecta models.

Pop III faint SN – reverse shock – unmixed ejecta models						
	HE1327−2326	HE1327−2326	HE0107−5240	HE0107−5240	SMSSJ031300	SMSSJ031300
	30 $M_\odot$	30 $M_\odot$	35 $M_\odot$	35 $M_\odot$	80 $M_\odot$	80 $M_\odot$
	A	B	A	B	A	B
			rev1			
M_{AC}	–	7.54×10^{-4}	6.20×10^{-2}	5.88×10^{-5}	–	7.19×10^{-2}
			rev2			
M_{AC}	–	1.54×10^{-4}	6.20×10^{-2}	1.54×10^{-5}	–	1.39×10^{-2}
			rev3			
M_{AC}	–	1.02×10^{-4}	6.20×10^{-2}	–	–	8.65×10^{-3}

This paper has been typeset from a TEX/LATEX file prepared by the author.